Aalto University
School of Science

Master's Programme in Engineering Physics

Flat-band-based optical switching in a Stub unit cell

Jere Haavisto

Master's Thesis
2025

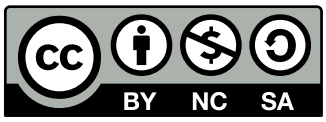

Aalto University
School of Science

Author Jere Haavisto

Title Flat-band-based optical switching in a Stub unit cell

Degree programme Engineering Physics

Major Materials Physics and Quantum Technology

Supervisor Prof. Päivi Törmä

Advisors Dr Grazia Salerno, Dr Javier Cuerda

Date July 31, 2025 **Number of pages** 45 **Language** English

Abstract

Optical switching plays a crucial role in the development of high-speed photonic technologies, offering the potential for ultrafast and low-power signal processing. Among various techniques under investigation, flat band systems have emerged as promising candidates due to their ability to support localized states arising from destructive interference. This thesis explores the Stub unit cell as a platform for realizing interference-based optical switching.

The proposed switch operates in the "ON" and "OFF" states by modulating photon interactions. In the "OFF" state, a single photon remains localized due to destructive interference. When a second photon is introduced into the system, interactions induce delocalization, transitioning the switch to the "ON" state. We examine both closed and open dynamic regimes: in closed dynamics, the particle number is conserved, while in open dynamics, a sink continuously reduces the particle number. Analytical and numerical methods, including exact diagonalization and Lindblad master equations, are used to evaluate the dynamics and optimize performance.

The objective of this thesis is to identify the optimal inter-site spacing that minimizes the switching time of the three-site switch. The switching time is extracted from the simulations as a function of the hopping amplitude between the sites. The optimal spacing is determined using the eigenfrequency analysis of dielectric pillars, where the eigenmodes are simulated to relate the hopping amplitude to the physical distance, allowing us to identify the configuration that yields the fastest switching response.

The results highlight the potential of flat band-induced localization for ultrafast optical switching. Although the proposed switch is limited to operation at the single-photon level and is not viable for practical use at the classical limit, it represents a significant conceptual advancement. Considering the rapid development in single-photon manipulation technologies, this switching mechanism could eventually be implemented in photonic crystal systems, opening new possibilities for innovative applications in quantum photonics.

Keywords optical switching, flat band, Stub lattice

Aalto-yliopisto
Perustieteiden
korkeakoulu

Tekijä Jere Haavisto

Työn nimi Litteään energiavyöhön perustuva optinen kytkin Stub-hilan yksikkösolussa

Koulutusohjelma Engineering Physics

Pääaine Materials Physics and Quantum Technology

Työn valvoja Prof. Päivi Törmä

Työn ohjaajat Dr Grazia Salerno, Dr Javier Cuerda

Päivämäärä 31.07.2025 **Sivumäärä** 45 **Kieli** englanti

Tiivistelmä

Tässä diplomityössä tutkitaan litteän energiavyön potentiaalia täysin optiseen kytkimeen keskittymällä Stub-hilamalliin. Litteät energiavyöt tarkoittavat dispersiottomia vöitä, joissa tilan energia ei riipu partikkelin liikemäärästä. Nämä vyöt mahdollistavat destruktiivisen interferenssin aikaansaamat lokalisoituneet ominaistilat. Nämä erityislaatuiset tilat tarjoavat kiinnostavia ominaisuuksia optisen kytkimen näkökulmasta. Työssä hyödynnetään Bose-Hubbard-mallia tarkasteltaessa destruktiivisen interferenssin ja vuorovaikutusten aiheuttaman delokalisaation välistä kombinaatiota. Tämä kombinaatio muodostaa ehdotetun kytkimen perustan.

Kytkin toimii "ON"- ja "OFF"-tiloissa moduloimalla fotonien välisiä vuorovaikutuksia. "OFF"-tilassa yksittäiset fotonit pysyvät lokalisoituneina destruktiivisen interferenssin vuoksi. Kun järjestelmään lisätään toinen kontrollifotoni, vuorovaikutukset johtavat delokalisaatioon ja kytkin siirtyy "ON"-tilaan. Työssä tarkastellaan sekä suljetun että avoimen dynamiikan systeemejä: suljetussa systeemissä hiukkasten lukumäärä säilyy, kun taas avoimessa systeemissä hiukkasia poistetaan jatkuvasti ulostulopisteestä. Dynaamista käyttäytymistä analysoidaan sekä analyyttisesti että numeerisesti hyödyntämällä eksaktia diagonaalisaatiota ja Lindbladin yhtälöitä.

Tämän työn tavoitteena on löytää optimaalinen etäisyys Stub-hilan yksikkösoluun perustuvan kytkimen hilapisteiden välille, jotta kytkentänaika olisi mahdollisimman lyhyt. Kytkentäaika määritetään simulaatioista tutkimalla sen riippuvuutta hilapisteiden väliseen tunnelointienergiaan. Optimaalinen etäisyys selvitetään dielektristen pilarien ominaistaajuusanalyysin kautta, jossa simuloidaan systeemin ominaistiloja. Näin voidaan yhdistää tunnelointienergia fyysiseen etäisyyteen ja löytää hilapisteiden välinen etäisyys, joka tuottaa nopeimman kytkentäajan.

Tulokset osoittavat, että litteissä energiavöissä esiintyvällä lokalisaatiolla on merkittävä potentiaali nopeissa ja vähäenergisissä optisissa kytkimissä. Vaikka ehdotettu malli toimii yksittäisfotonitasolla eikä ole soveltuva käytettäväksi makroskooppisella valolla, se edustaa tärkeää käsitteellistä edistysaskelta. Kun yksittäisfotoniteknologia kehittyy edelleen, tällaisella kytkentämekanismilla voi tulevaisuudessa olla merkittävä rooli uusissa kvanttifotoniikan sovelluksissa.

Avainsanat optinen kytkentä, litteä energiavyö, Stub-hila

Contents

1 Introduction

Photonics, the use of photons for information processing, presents a promising approach to overcoming the speed and bandwidth limitations of traditional electronics. By replacing electrons with photons in computational circuits, one can, in principle, achieve higher data transmission rates and processing speeds with lower energy dissipation [1]. A critical element in any computing system is a switch that controls the flow of signals. In optical computing, an all-optical switch serves as a transistor or logic gate, controlling the signal by using only photons. All-optical switches eliminate the need for optical-to-electronic conversion. This process in current networks adds latency and energy usage as optical signals are converted to electrical form and back. The development of ultrafast, low-power optical switches is therefore a key step toward integrated photonic circuits and quantum optical computing platforms.

Achieving all-optical switching at the fundamental limit of single or a few photons is challenging because photons ordinarily do not interact with each other. Conventional optical switching schemes often rely on nonlinear materials and high intensities, for example, exploiting the Kerr effect in silicon photonics to induce an effective photon–photon interaction [1]. One approach is to enhance photon–photon interactions using optical resonators or waveguides that confine light and prolong the interaction time [1]. In addition to strengthening photon-photon interactions, one approach is to engineer lattices such that even inherently weak nonlinearities can cause a significant change in the propagation of light.

Flat band photonic lattices provide a particularly intriguing platform for such an approach. A flat band is an energy band in a periodic system that is completely dispersionless (momentum independent). In a photonic flat band, the group velocity of a photon is essentially zero, and its wavefunction can be localized in space as a compact localized state (CLS) confined to a small cluster of lattice sites. This localization arises from destructive interference: by design of the lattice geometry, the amplitude of the optical field on specific sites cancels out the propagation into neighboring sites [2]. As a result, a single photon placed in a flat band will remain trapped in a local region and will not propagate through the lattice. This interference-based localization is achieved without any external potential or disorder; it is a linear wave phenomenon arising from the symmetry and connectivity of the lattice [2]. Such trapped photon states can represent the "OFF" state of an optical switch, since light is prevented from reaching the output ports.

A remarkable property of flat-band systems is that when the usual kinetic energy is extinguished, even very weak interactions become significant in determining the behavior of the system [3]. In other words, the absence of dispersion means that the energy scale of photon–photon interactions, however small, is no longer overshadowed by propagation. Importantly for switching, it has been shown that while single-particle states remain localized, two-particle states can become delocalized due to the interaction between photons. This interplay between interference-induced localization and interaction-induced delocalization promotes a novel all-optical switching mechanism [4]. Essentially, a single photon alone stays trapped, but the arrival of an additional control photon enables the pair of photons to redistribute over the lattice. The control

photon "unlocks" the signal photon from its trapped state, allowing it to propagate to the output waveguides. This single-photon-by-single-photon switching concept operates at the quantum level, offering extremely low switching energies and potentially ultrafast switching times, ultimately limited by the timescale of photon hopping and interaction in the medium [4].

In this thesis, we explore this switching concept using the simplest flat-band lattice that supports interference localization: the unit cell of a Stub lattice. The Stub lattice consists of three coupled sites and is known to exhibit one flat band in its band structure [2]. In a photonic implementation, these sites can be realized as three high-index dielectric pillars or resonators arranged optimally with one another. In practical terms, a single photon injected into the input site can be confined there, with no optical power reaching the other sites due to destructive interference. We identify this localized one-photon state as the "OFF" state of the switch. When a second photon is introduced into the input site, the nonlinear interaction (specifically, the Kerr nonlinearity in the dielectric material) effectively breaks the interference condition. The two-photon state is then no longer a stationary localized mode. The result is that the pair of photons delocalizes across the lattice, with the photons exiting through the output pillars. This two-photon state corresponds to the "ON" state in our scheme. Thus, the Stub lattice provides a minimal, conceptually straightforward model of an all-optical switch where photon localization via a flat band represents the "OFF" condition, and photon delocalization via interaction represents the "ON" condition.

The primary goal of this research is to determine how to achieve the fastest possible switching time in the three-site model. The switching time depends on how quickly the two-photon state can spread from the input site to the output sites, which in turn is influenced by the lattice coupling strengths and the photon–photon interaction strength. We investigated these factors by modeling the system with the Bose–Hubbard Hamiltonian and simulating the dynamical evolution of one- and two-photon states. A key tunable parameter in a physical realization is the inter-site distance between the dielectric pillars, which controls the coupling (hopping amplitude) between the sites. By varying the inter-pillar distance, we can tune the hopping amplitude. There is an anticipated trade-off, as extremely weak coupling traps the photon too effectively, resulting in slow or no switching.

In contrast, overly strong coupling may undermine the flat-band localization condition. Through systematic simulations, we identify an optimal coupling regime and thus an optimal physical spacing that yields minimal switching time. We studied both closed (conserved particle number) and open operations (photons depleted from the output site) to evaluate how dissipation or photon extraction might influence the switching speed and efficiency.

Section 2 of this thesis reviews the relevant background, beginning with the principles of optical switching and existing platforms for all-optical switches, and then introducing the concept of flat bands and interference-based localization in photonic lattices. Section 3 presents the theoretical framework for our study, introducing the Bose–Hubbard model to describe interacting photons at lattice sites and explaining the mechanisms of photon localization and interaction-induced delocalization. In Section 4, we describe the computational methods and tools used in the work. Section

5 details the simulation results and analysis of the three-site switch. We compare the behavior of a single photon versus a two-photon pair in the three-site model, under both closed and open conditions, and evaluate the switching time and photon transport for different inter-site distances and interaction strengths. We identify the optimal lattice configuration that minimizes the switching time and discuss the physical implications of this design. Finally, Section 6 concludes the thesis with a summary of the main findings and their significance. We highlight the potential of flat-band-based optical switching for future photonic technologies and discuss remaining challenges and possible directions for further research.

2 Background

2.1 Optical switching

Ultrafast optical computing, aiming to utilize photons as carriers of information, represents a significant advancement in integrated photonic technology [5]. The prerequisite for continuing development is the ability to modulate the propagation of photons using only photons, i.e., optical switching. Analogously to electronic switching, all-optical switching enables the control-light-induced activation or deactivation of signal light, effectively enabling ON/OFF conversion.

Optics and electronics exhibit fundamentally different characteristics that can be qualitatively categorized into two main distinctions [1]. First, optical signals operate at wavelengths much shorter than those of electronic ones, typically in the nanometer range. This has important implications for device design: waveguide structures used in optical communication and computing are usually on the order of the optical wavelength, enabling efficient confinement and guidance of light through dielectric materials. Additionally, the short wavelength of light enables free-space optical techniques to manipulate multiple beams simultaneously within a compact spatial domain, facilitating high-throughput and parallel signal processing [1].

The second key distinction arises from quantum mechanics. Whereas electronic systems typically use classical detection methods based on voltage measurements, optical systems rely on quantum detection techniques, most notably photon counting [6]. This approach to detection enables the precise and efficient manipulation of light at the quantum level.

The continuous advancement of all-optical computing is driving fresh exploration in various domains, including silicon photonics [7], organic photonics [8], nanophotonics [9], and plasmonic structures [10]. In silicon photonics, silicon acts as an optical medium, where light propagation is governed by nonlinear optical effects such as the Kerr effect, two-photon absorption, and the Raman effect [1]. Organic photonics opens up new possibilities for developing flexible, cost-effective optical components with tunable wavelengths, while plasmonic structures make it possible to confine and manipulate light at the nanoscale, which is key to building compact and ultrafast optical devices.

Nonlinear optics is the enabling physics behind all-optical switching. The primary mechanism in most switches is the optical Kerr effect, in which the refractive index n changes proportionally to the light intensity:

$$n = n_0 + n_2 I.$$

Here, n_2 is the nonlinear index coefficient [5]. For example, fused silica has $n_2 \sim 3 \times 10^{-20} \mathrm{m}^2/\mathrm{W}$, so very high intensities are needed for a noticeable index shift [11]. Thus, practical devices utilize materials with orders of magnitude larger n_2 (such as chalcogenide glass, gallium arsenide and organics), and combine them with tight field confinement to maximize I. Because the Kerr response is essentially instantaneous and lossless, it can support femtosecond switching [12].

The practical implementation of all-optical switching involves the construction of sophisticated devices using photonic or plasmonic micro/nanostructures embedded with nonlinear optical materials [5]. These structures, such as nonlinear photonic crystals (PCs) and PC nanocavities [13][14], nonlinear metamaterials/metasurfaces [15], nonlinear dielectric ring nanocavities [16], and nonlinear plasmonic nanocavities [17], serve as the framework for realizing all-optical switching capabilities.

Photonic crystals are widely used in optical switching schemes. These microstructured materials are characterized by a periodic dielectric constant, which enables them to manipulate electromagnetic waves through spatially varying refractive indices. This periodicity gives rise to one of their most defining features: the photonic bandgap; a frequency range within which the propagation of electromagnetic waves is strictly forbidden due to the absence of available photonic states [5]. The bandgap in photonic crystals forms as a result of Bragg scattering, where light waves reflect off the periodic layers and interfere with each other. At specific frequencies, this interference is destructive, blocking the light from passing through and creating a range of wavelengths where transmission is effectively suppressed.

By introducing defects into the periodic lattice, it is possible to localize light in the form of photonic crystal nanocavities, which support discrete resonant modes within the photonic bandgap [5]. These localized modes enable strong field confinement and selective transmission at target wavelengths. Furthermore, one can dynamically modulate the photonic band structure of the crystal by using nonlinear optical materials. Changes in the local refractive index, such as those induced by optical Kerr nonlinearity, can shift either the band edge or the resonance condition of nanocavities. As a result, all-optical switching in photonic crystals can be achieved via two main mechanisms: the stop-band shift and the nanocavity mode shift. Among these, the latter is more widely employed due to practical challenges in engineering sharp and tunable band edges. At the same time, nanocavities offer a more straightforward and robust platform for high contrast switching [18].

2.2 Flat bands

An energy band in a periodic system describes the energy eigenvalues that particles can possess in a system. Energy is typically presented as a function of momentum k. A flat band, also known as a dispersionless band, is an energy band that is entirely independent of momentum k. From the k independence it follows that all the eigenstates of a flat band are degenerate. This distinctive feature yields intriguing physical properties and emergent phenomena that have garnered significant attention from researchers in recent years. Flat-band lattices that have been widely researched include the Dice lattice, Lieb lattice, Kagome lattice, and Stub lattice [19].

Since energy is not dependent on momentum, flat bands are susceptible to perturbations; even the weakest perturbation can have a significant influence on a flat band state, changing its transport properties. Thus, flat bands are unstable against generic perturbations. Keeping perfectly flat bands requires either tuning of system parameters or protection by lattice symmetry [19].

The study of flat-band models originally arose from Sutherland's observation of a

flat band [20]. He noticed "strictly localized states" in a Dice lattice. Subsequently, Lieb presented an edge-centered square lattice known as the Lieb lattice [19]. Soon after, Mielke and Tasaki separately extended this concept to encompass examples of flat band ferromagnetism, which manifests when the lowest single-particle energy band remains flat [21][22]. Mielke's approach to constructing flat-band lattices relied on line graphs, a technique that involves elevating the links of a standard lattice to individual lattice sites.

In contrast, Tasaki's "decorated" lattices produce flat bands through the interplay of finely balanced nearest- and next-nearest-neighbor hopping interactions. In each scenario, the researchers immediately recognized that the extensive degeneracy of the flat band enables the creation of tightly localized Wannier-like eigenstates [19]. These states form through linear combinations of extended Bloch states. Crucially, flat-band modes in photonic lattices take the form of compact localized states (CLS). By design of the lattice geometry, the field amplitudes cancel at specific sites, confining the mode to a small cluster of resonators or waveguides. For example, in a one-dimensional Stub lattice (three sites per unit cell), the isolated flat-band mode has a nonzero amplitude only at the two outer sites of a cell, with destructive interference at the middle site [2]. As a result, a photon in that mode remains localized in one unit cell. Similarly, in a two-dimensional Lieb lattice, each flat-band eigenmode occupies only four sites of a unit cell, forming a compact localized "cross" shape [23][24]. These CLSs are exact linear modes of the lattice – they exist without any external disorder or defect, purely due to the lattice symmetry [24]. In all known flat-band lattices, one can construct such compact solutions that remain strictly confined under linear propagation. The CSL formation schematics for both a Stub and a Lieb lattice are presented in Figures 1a and 1b, respectively.

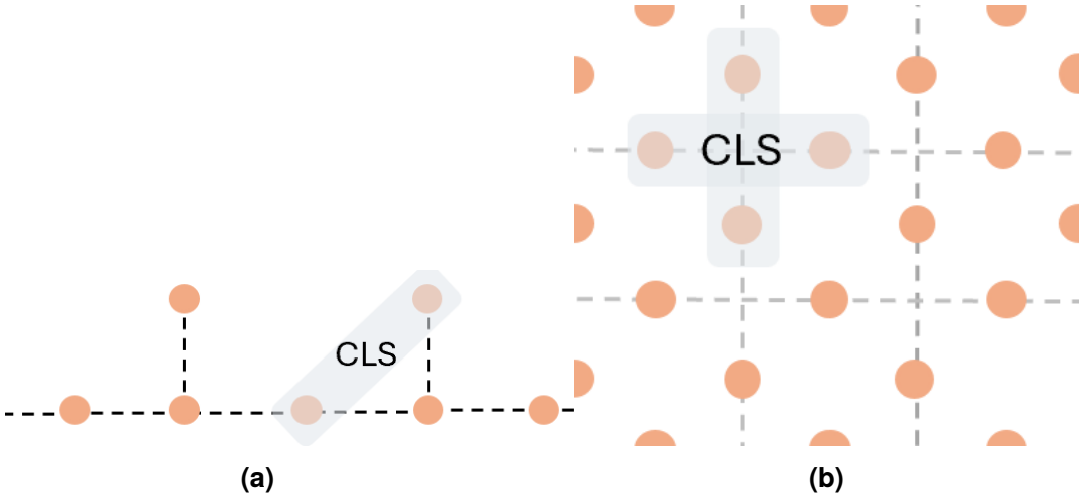

Figure 1: Schematic of the compact localized state formation in **(a)** a Stub lattice **(b)** a Lieb lattice.

Today, flat bands have garnered significant attention across a range of cutting-edge applications because of their unique ability to support strongly correlated and highly localized states. One prominent area is superconductivity, in which electrons

form Cooper pairs that can flow without resistance. The enhancement of interaction effects in flat bands could potentially enable high-temperature superconducting phases. Although it is not apparent that Cooper pairs can propagate in flat bands, it has been demonstrated that a supercurrent is achievable if the system possesses a nontrivial quantum geometry [25].

The physical significance of flat bands is apparent in photonic transport and switching. Since flat-band modes do not carry energy across the lattice, they effectively act as an "OFF" state for light: no power reaches other sites. Since flat bands are susceptible to even small perturbations, adding a weak photon–photon interaction breaks the perfect destructive interference that traps light, leading to an "ON" state.

3 Theory

In this section, we study the theory of photonic switching, starting with the Bose-Hubbard model, which describes the behavior of photons in a lattice. We will use the results of solid-state physics to study the properties of the Stub lattice. Finally, we present optical modes in dielectric particles. In the following sections, we set $\hbar = 1$ for straightforward equations.

3.1 The Bose-Hubbard model

We use the spinless Bose-Hubbard model to describe the behavior of interacting photons in a Stub lattice. The Bose–Hubbard model employs the tight-binding approximation, which is valid under the assumption that particle interactions are short-range and occur only between particles localized at the same lattice site.

We begin by introducing the bosonic annihilation and creation operators $\hat{a}_i$ and $\hat{a}_i^\dagger$, which, respectively, remove and add a photon at site i. These operators obey the canonical bosonic commutation relation:

$$[\hat{a}_i, \hat{a}_j^\dagger] = \hat{a}_i \hat{a}_j^\dagger - \hat{a}_j^\dagger \hat{a}_i = \delta_{ij} \tag{1}$$

The general Bose-Hubbard model is defined as:

$$\hat{H} = \sum_i \epsilon_i \hat{n}_i - \sum_{\langle i,j \rangle} t_{ij} \hat{a}_i^\dagger \hat{a}_j + \sum_i U_i \hat{n}_i (\hat{n}_i - 1)/2 \tag{2}$$

where i labels the lattice sites, ϵ_i refers to the site potential, and $\hat{n}_i = \hat{a}_i^\dagger \hat{a}_i$ are the particle number operators. The hopping energy t_{ij} denotes the likelihood that a particle will tunnel to a neighboring site, and $\langle i, j \rangle$ denotes the summation over neighboring sites. Additionally, U_i describes the on-site interaction strengths between two photons.

3.2 Stub lattice

We now analyze how photons propagate within a Stub lattice, shown in Fig. 2a. The unit cell consists of three sites: A, B, and C. In a Stub lattice, particle hopping between sites A and B is prohibited, that is, $t_{\mathrm{AB}} = 0$. Without interactions, the periodic 1D Stub lattice is described by the Bose-Hubbard Hamiltonian as:

$$H = \sum_j \epsilon_{\mathrm{A}} \hat{a}_j^\dagger \hat{a}_j + \epsilon_{\mathrm{B}} \hat{b}_j^\dagger \hat{b}_j + \epsilon_{\mathrm{C}} \hat{c}_j^\dagger \hat{c}_j - t_{\mathrm{AC}} (\hat{a}_j^\dagger \hat{c}_j + \hat{a}_{j+1}^\dagger \hat{c}_j + \mathrm{H.c.}) - t_{\mathrm{BC}} (\hat{b}_j^\dagger \hat{c}_j + \mathrm{H.c.}) \tag{3}$$

where ϵ_{A}, ϵ_{B} and ϵ_{C} are the on-site potentials at sites A, B, and C, and the hopping energies are t_{AC} between sites A and C, and t_{BC} between sites B and C. H.c. stands for Hermitian conjugate.

We begin by determining the eigenenergies and eigenstates of a periodic Stub lattice composed of N_c unit cells. Each unit cell contributes three eigenstates to the

system. A detailed derivation of the eigenenergies and the corresponding eigenstates is provided in Appendix A. Setting $\epsilon_A = \epsilon_B = \epsilon_C = 0$, we obtain the eigenenergies as

$$E_k = \begin{cases} -\sqrt{t_{\mathrm{BC}}^2 - 2t_{\mathrm{AC}}^2(1+\cos(ka))} \\ 0 \\ \sqrt{t_{\mathrm{BC}}^2 - 2t_{\mathrm{AC}}^2(1+\cos(ka))}. \end{cases} \tag{4}$$

Fig. 2b presents these three energy bands. The middle band is entirely dispersionless, resulting in degeneracy among its eigenstates. These flat-band eigenstates correspond to spatially localized modes.

$$|\psi_{\mathrm{FL,j}}\rangle = [-\frac{t_{\mathrm{AC}}}{t_{\mathrm{BC}}}\hat{b}_{j-1}^{\dagger} + \hat{a}_j^{\dagger} - \frac{t_{\mathrm{AC}}}{t_{\mathrm{BC}}}\hat{b}_j^{\dagger}]\,|0\rangle \tag{5}$$

The flat band states maintain their localization because of destructive interference caused by the opposite signs of the amplitudes. The lower and higher bands are completely dispersive delocalized states.

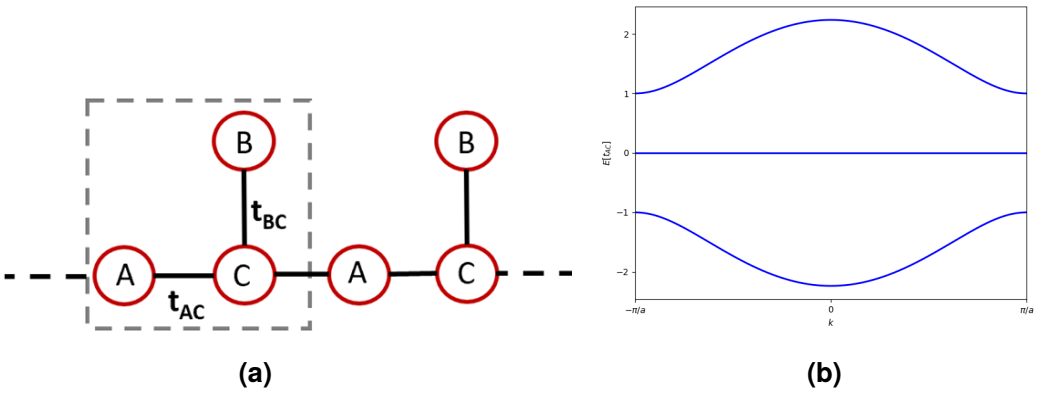

Figure 2: **(a)** Schematic of the Stub lattice. Each unit cell (grey box) comprises three lattice sites. t_{AC} and t_{BC} are the hopping amplitudes between the sites. **(b)** Band structure of an infinite Stub lattice.

While the infinite periodic Stub lattice provides valuable insight into the emergence of flat bands and their corresponding localized eigenstates, practical implementations and switching operations are inherently finite in size. Therefore, we now turn our attention to a single unit cell of the Stub lattice with open boundary conditions. Even in this truncated geometry, the system continues to support localized eigenstates resulting from destructive interference. This feature makes the unit cell an ideal minimal model for exploring the fundamental switching mechanism enabled by interaction-induced delocalization.

3.3 Closed dynamics

We will now inspect the behavior of photons in a three-site model with closed dynamics. The closed-case three-site system is presented in Fig. 3. Site A serves as the input location, whereas the output is observed at sites B and C. Sections 3.3 and 3.4 are based on reference [4].

Hamiltonian of the Stub unit cell can be written in matrix form as:

$$H_{0,\text{unit cell}} = \begin{pmatrix} \epsilon_A & 0 & -t_{\text{AC}} \\ 0 & \epsilon_B & -t_{\text{BC}} \\ -t_{\text{AC}} & -t_{\text{BC}} & \epsilon_C \end{pmatrix},$$

where we can set $\epsilon_B = 0$ without loss of generality.

It is evident that localizing the excitation at a single site, such as site A, leads to the decoupling of neighboring sites ($t_{CA} = 0$). Representing the two-site localized eigenstate as

$$|loc\rangle = (\alpha_{loc}, \beta_{loc}, 0) \tag{6}$$

leads to three simultaneous determinant equations. A nontrivial solution is obtained by setting

$$\epsilon_A = t_{\text{AB}}\left(\frac{t_{\text{BC}}}{t_{\text{AC}}} - \frac{t_{\text{AC}}}{t_{\text{BC}}}\right) = 0 \tag{7}$$

By inserting $\epsilon_C = 0$, we obtain the following from the eigenvalue equation: $-E(E^2 - (t_{\text{AC}}^2 + t_{\text{BC}}^2) = 0$. This equation has roots

$$\begin{aligned} E_{\text{loc}} &= 0, \\ E_{\pm} &= \pm t_{\text{AC}}\sqrt{r_{\text{AB}}^2 + 1} = \pm\Delta, \end{aligned} \tag{8}$$

where the first is the energy of the localized state, and the second is the energy of the delocalized states. Furthermore, to have a localized state at two sites of the form 6, the amplitudes at sites A and B must adhere to the following condition:

$$r_{\text{AB}} \equiv \frac{\alpha_{loc}}{\beta_{loc}} = -\frac{t_{\text{BC}}}{t_{\text{AC}}}, \tag{9}$$

where r_{AB} is the defined ratio.

Since $|loc\rangle = (\alpha_{loc}, \beta_{loc}, 0)$ and $r_{\text{AB}} = \frac{\alpha_{loc}}{\beta_{loc}}$, we find from normalization that this state must satisfy $|\alpha_{loc}|^2 + |\beta_{loc}|^2 = 1$. Therefore, $|\alpha_{loc}| = \frac{|r_{\text{AB}}|}{\sqrt{1+r_{\text{AB}}^2}}$ and $|\beta_{loc}| = \frac{1}{\sqrt{1+r_{\text{AB}}^2}}$. One can express the states as:

$$|loc\rangle = \frac{1}{\sqrt{1 + r_{\text{AB}}^2}}(r_{\text{AB}}, 1, 0) \tag{10}$$

$$|+\rangle = \frac{1}{\sqrt{2(1 + r_{\text{AB}}^2)}}(-1, r_{\text{AB}}, \sqrt{1 + r_{\text{AB}}^2}) \tag{11}$$

$$|-\rangle = \frac{1}{\sqrt{2(1 + r_{\text{AB}}^2)}}(-1, r_{\text{AB}}, -\sqrt{1 + r_{\text{AB}}^2}) \tag{12}$$

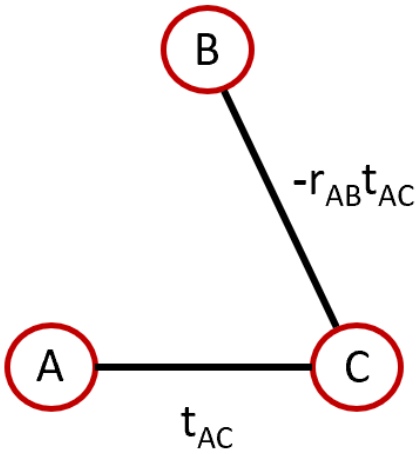

Figure 3: The Stub unit cell with closed dynamics. Input is applied to site A, while site C serves as the output. The hopping amplitude between sites A and B is equal to zero.

The switch enters the "ON" state when two photons are initially present at site A, $|A, A\rangle = b_A^\dagger b_A^\dagger |0\rangle$. This state can be expressed as follows:

$$\begin{aligned} |A, A\rangle = &\langle loc|A\rangle^2 |loc, loc\rangle + \langle +|A\rangle^2 |+, +\rangle + \langle -|A\rangle^2 |-, -\rangle \\ &+ 2\langle loc|A\rangle \langle +|A\rangle |loc, +\rangle + 2\langle loc|A\rangle \langle -|A\rangle |loc, -\rangle \\ &+ 2\langle +|A\rangle \langle -|A\rangle |+, -\rangle \end{aligned} \tag{13}$$

Since the site basis state is just $|A\rangle = (1, 0, 0)$, we obtain the normalized initial state as:

$$\begin{aligned} |A, A\rangle = \frac{1}{1 + r_{\mathrm{AB}}^2} \big(& r_{\mathrm{AB}}^2 |loc, loc\rangle + r_{\mathrm{AB}} |loc, +\rangle + r_{\mathrm{AB}} |loc, -\rangle + \frac{1}{2} |+, +\rangle \\ & + \frac{1}{2} |-, -\rangle + \frac{1}{\sqrt{2}} |+, -\rangle \big) \end{aligned} \tag{14}$$

The non-interacting energy spectrum has a gap Δ; the eigenstates $|loc, loc\rangle$ and $|+, -\rangle$ lie at zero energy, while the other two-particle product states lie at different energies. For small interactions $U << t_{\mathrm{AC}}\sqrt{r_{\mathrm{AB}} + 1}$ compared to Δ, transitions to higher energy states are suppressed [4]. This suppression justifies projecting the full Hamiltonian into the two-dimensional subspace spanned by $|loc, loc\rangle$ and $|+, -\rangle$ through the Schrieffer-Wolff transformation. When r_{AB} is large, the input state is well approximated by $|loc, loc\rangle$, and the output state corresponds to $|+, -\rangle$. This system can be expressed with the following Hamiltonian: [4]

$$H_{\mathrm{eff}} = \frac{U}{(1 + r_{\mathrm{AB}}^2)^2} \begin{pmatrix} 1 + r_{\mathrm{AB}}^2 + r_{\mathrm{AB}}^4 & \sqrt{2} r_{\mathrm{AB}}^2 \\ \sqrt{2} r_{\mathrm{AB}}^2 & 1 + r_{\mathrm{AB}}^4 \end{pmatrix}$$

Here, the energy detuning between the two states δ and their mutual overlap t_{12} are given by

$$\delta = \frac{U r_{\mathrm{AB}}^2}{(1 + r_{\mathrm{AB}}^2)^2} \tag{15}$$

$$t_{12} = \frac{\sqrt{2} U r_{\mathrm{AB}}^2}{(1 + r_{\mathrm{AB}}^2)^2}. \tag{16}$$

The state dynamics of this kind of two-level system consists of Rabi oscillations that have a frequency [4]

$$\Omega = \sqrt{(\delta/2)^2 + |t_{12}|^2} = \frac{3}{2} \frac{U r_{\mathrm{AB}}^2}{(1 + r_{\mathrm{AB}}^2)^2}. \tag{17}$$

The switching time is defined as the half-period of the associated Rabi oscillation:

$$t_{\mathrm{switch}} = \frac{\pi}{2\Omega} = \frac{\pi (1 + r_{\mathrm{AB}}^2)^2}{3 U r_{\mathrm{AB}}^2}. \tag{18}$$

In this effective two-level system, the Hamiltonian has two eigenstates $|loc, loc\rangle$ and $|+, -\rangle$. The probability of measuring a single or a pair of photons at the output, corresponding to the "ON" state of the switch, is given by:

$$P_{\mathrm{ON}} = \frac{|t_{12}|^2 \sin^2(\Omega t)}{\Omega^2} = \frac{|t_{12}|^2}{\Omega^2}, \tag{19}$$

where in the second equality, we present the probability at $t = t_{\mathrm{switch}}$. Inserting the expressions from Equations 15, 16 and 17, we obtain the probability $P_{\mathrm{ON}} = 8/9$.

When a single photon is initially placed at site A, representing the "OFF" state, it remains strongly localized there. However, there is a finite probability of finding the photon at the output sites [4]:

$$P_{\langle OFF \rangle} = \frac{1/2 + 2 r_{\mathrm{AB}}^2}{(r_{\mathrm{AB}}^2 + 1)^2}. \tag{20}$$

This is the same probability as finding the photon localized at the input site in the two-photon interacting case. Therefore, the switch has an "OFF" state leakage probability, which is presented with other results in Fig. 5a. From Eq. 20, we see that the ratio r_{AB} can be increased to minimize the "OFF" state leakage. However, in that case, the switching time also increases, as can be seen in Eq. 18.

3.4 Open dynamics

The open dynamics of the system can not be modeled using a Bose-Hubbard model, but one has to utilize a Lindblad master equation, which governs the time evolution of the density operator $\hat{\rho}$ [4].

$$\frac{d}{dt}\hat{\rho} = -\frac{i}{\hbar}[\hat{H}, \hat{\rho}] + \sum_n \gamma_n (\hat{L}_n \hat{\rho} \hat{L}_n^\dagger - \frac{1}{2}\hat{L}_n^\dagger \hat{L}_n, \hat{\rho}) \tag{21}$$

Here, the first term represents the unitary evolution governed by the system Hamiltonian $\hat{H}$, while the second term accounts for dissipative processes, where $\hat{L}_n$ are the ladder operators and γ_n denote the decay rates into an external reservoir. To model open system dynamics, we introduce a loss channel at site C, thus $\hat{L} = \hat{a}_C$ and γ is the decay rate of that site; see Fig. 4.

In the "OFF" state, a single photon is confined near site A, similar to the closed dynamics. Due to localization, there is a high probability of finding a single photon in the system despite the sink. This behavior can be seen in the results, as shown in Figures 10a and 10b.

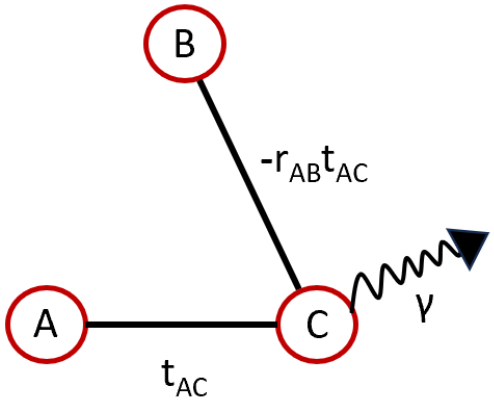

Figure 4: Three-site system with open dynamics. The system is driven from site A, with site C serving as the output via a decay channel characterized by rate γ.

In the presence of interactions, the "ON" state of the system evolves similarly to the closed case, with the key difference that the Rabi oscillations are suppressed by the decay rate γ. Over time, the photon pair eventually transitions into the decay channel, leading to depletion of the system. In consequence, the probability of observing two photons within the system, P_2, approaches zero over time. Meanwhile, the probability of observing a single photon remains finite because of the nonzero likelihood of a photon remaining localized at site A.

Unlike closed system operations, the open system switch can achieve arbitrarily high efficiency, in which the presence of a control photon ensures that a single photon leaves the system reliably [4]. To suppress the "OFF" signal, one can manipulate the ratio r_{AB}, effectively guiding the initial state toward localization. Enhancing the ratio substantially improves the contrast between the "ON" and "OFF" states. However, increasing r_{AB} also increases the switching time, as can be seen in Eq. 23. Therefore, the challenge is to find the optimal solution to obtain a minimal switching time with enough efficiency.

A key distinction of the open system scenario is that the switching time is significantly influenced by the decay rate γ, in contrast to the closed system, where

the time scale is governed primarily by Rabi oscillations. We define the switching time as the duration over which the probability of a photon leaving the system exceeds a predefined threshold of $1-\epsilon$, where $\epsilon = 10^{-3}$. It has two opposite behaviors in the range of small and large γ compared to the delocalization time scale. In the small-γ limit, the switching time becomes independent of the interaction strength and is given by [4]

$$t_{\text{switch}} = \frac{-9\ln(\epsilon)}{4\gamma}. \tag{22}$$

When γ is large, the particles exit the system rapidly. In this limit, one can approximate the decay channel site as being effectively unoccupied at all times. This approximation leads to [4]:

$$t_{\text{switch}} = -\frac{\ln(\epsilon)\gamma(1+r_{\text{AB}}^2)^4}{8r_{\text{AB}}^4 U^2} \tag{23}$$

We can see these theory lines for the switching time in closed and open dynamics with the data in Figures 6, 8c, and 9.

3.5 Optical modes in spherical particles

Subsequently, we will present the theory of optical modes in spherical particles. The energies of the eigenmodes are used in the estimation of the hopping term in the Bose-Hubbard model and can thus connect the theoretical model with real lattice structures.

For spherical particles, the scattering can be described using Lorentz-Mie theory [26]. These solutions allow one to express the field surrounding a scattering item as a function of the incident fields and to explain the light field dispersed by small spherical particles.

The field equations admit solutions that may be represented as infinite series using vector spherical harmonics [27]:

$$\begin{aligned}
\mathbf{M}_{emn} &= -\frac{m}{\sin\theta}\sin(m\phi)P_n^m(\cos\theta)z_n(\rho)\hat{\mathbf{e}}_\theta - \cos(m\phi)\frac{dP_n^m(\cos\theta)}{d\theta}z_n\hat{\mathbf{e}}_\phi,\\
\mathbf{M}_{omn} &= \frac{m}{\sin\theta}\cos(m\phi)P_n^m(\cos\theta)z_n(\rho)\hat{\mathbf{e}}_\theta - \sin(m\phi)\frac{dP_n^m(\cos\theta)}{d\theta}z_n\hat{\mathbf{e}}_\phi,\\
\mathbf{N}_{emn} &= \frac{z_n(\rho)}{\rho}\sin(m\phi)n(n+1)P_n^m(\cos\theta)z_n(\rho)\hat{\mathbf{e}}_r + \cos(m\phi)\frac{dP_n^m(\cos\theta)}{d\theta}\frac{1}{\rho}\frac{d}{d\rho}[\rho z_n(\rho)]\hat{\mathbf{e}}_\theta\\
&\quad - m\sin(m\phi)\frac{P_n^m(\cos(\theta)}{\sin(\theta)}\frac{1}{\rho}\frac{d}{d\rho}[\rho z_n(\rho)]\hat{\mathbf{e}}_\phi,\\
\mathbf{N}_{omn} &= \frac{z_n(\rho)}{\rho}\sin(m\phi)n(n+1)P_n^m(\cos\theta)z_n(\rho)\hat{\mathbf{e}}_r + \sin(m\phi)\frac{dP_n^m(\cos\theta)}{d\theta}\frac{1}{\rho}\frac{d}{d\rho}[\rho z_n(\rho)]\hat{\mathbf{e}}_\theta\\
&\quad + m\cos(m\phi)\frac{P_n^m(\cos(\theta)}{\sin(\theta)}\frac{1}{\rho}\frac{d}{d\rho}[\rho z_n(\rho)]\hat{\mathbf{e}}_\phi
\end{aligned} \tag{24}$$

Here m and n are the separation constants, r, θ and ϕ are the spherical polar coordinates, P_n^m are the associated Legendre functions of the first kind and z_n is any of the four spherical Bessel functions j_n, y_n, $h_n^{(1)}$, or $h_n^{(2)}$.

The incident electric field $E_i = E_0 e^{ikr\cos\theta}\hat{\mathbf{e}}_x$ can be expanded using vector spherical harmonics [27]:

$$\begin{aligned} E_i &= \sum_{m=0}^{\infty}\sum_{n=m}^{\infty}(B_{emn}\mathbf{M}_{emn} + B_{omn}\mathbf{M}_{omn} + A_{emn}\mathbf{N}_{emn} + A_{omn}\mathbf{N}_{omn}) \\ &= \sum_{n=1}^{\infty}(B_{o1n}\mathbf{M}_{o1n}^{(1)} + A_{e1n}\mathbf{N}_{e1n}^{(1)}) = E_0\sum_{n=1}^{\infty} i^n \frac{2n+1}{n(n+1)}(\mathbf{M}_{o1n}^{(1)} - i\mathbf{N}_{e1n}^{(1)}). \end{aligned} \tag{25}$$

Here, the second equality follows from the orthogonality of the vector spherical harmonics [27] and is inferred in Appendix B. The radial dependence of the generating functions is specified as j_n by the superscript (1) on the vector spherical harmonics.

The incident magnetic field is derived by taking the curl of the incident electric field 25.

$$H_i = -\frac{k}{\omega\mu}E_0\sum_{n=1}^{\infty} i^n \frac{2n+1}{n(n+1)}(\mathbf{M}_{e1n}^{(1)} + i\mathbf{N}_{o1n}^{(1)}), \tag{26}$$

where k is the wave number in the medium, μ is the permeability of the medium, and ω represents the angular frequency of the incident electromagnetic wave.

Likewise, the scattered (E_s, H_s) and internal electromagnetic fields (E_1 and H_1) may be expressed through similar expansions. The expansion of the internal field (E_1 and H_1) is given as [27]:

$$\begin{aligned} E_1 &= \sum_{n=1}^{\infty} E_n(c_n\mathbf{M}_{o1n}^{(1)} - id_n\mathbf{N}_{e1n}^{(1)}), \\ H_1 &= -\frac{k_1}{\omega\mu_1}\sum_{n=1}^{\infty} E_n(d_n\mathbf{M}_{e1n}^{(1)} + ic_n\mathbf{N}_{o1n}^{(1)}), \end{aligned} \tag{27}$$

where $E_n = i^n E_0 \frac{2n+1}{n(n+1)}$, k_1 is the wave number inside the sphere and μ_1 is the permeability of the sphere.

The expansion of the scattered field is given as [27]:

$$\begin{aligned} E_s &= \sum_{n=1}^{\infty} E_n(ia_n\mathbf{N}_{e1n}^{(3)} - b_n\mathbf{M}_{o1n}^{(3)}), \\ H_1 &= \frac{k}{\omega\mu}\sum_{n=1}^{\infty} E_n(ib_n\mathbf{N}_{o1n}^{(3)} + a_n\mathbf{M}_{e1n}^{(3)}), \end{aligned} \tag{28}$$

where the superscript (3) specifies the radial dependence of the generating functions as $h_n^{(1)}$.

The vector spherical harmonics correspond to the electromagnetic eigenmodes of the spherical particle. The overall field is typically constructed as a linear combination

of these modes, weighted by the coefficients a_n, b_n, c_n and d_n. From the boundary conditions $(E_i + E_s - E_1) \times \hat{\mathbf{e}}_r = (H_i + H_s - H_1) \times \hat{\mathbf{e}}_r = 0$ one may solve all the scattering coefficients: [27]

$$\begin{aligned} a_n &= \frac{\mu m^2 j_n(mx)[x j_n(x)]' - \mu_1 j_n(x)[mx j_n(mx)]'}{\mu m^2 j_n(mx)[x h_n^{(1)}(x)]' - \mu_1 h_n^{(1)}(x)[mx j_n(mx)]'}, \\ b_n &= \frac{\mu_1 j_n(mx)[x j_n(x)]' - \mu j_n(x)[mx j_n(mx)]'}{\mu_1 j_n(mx)[x h_n^{(1)}(x)]' - \mu h_n^{(1)}(x)[mx j_n(mx)]'}, \end{aligned} \tag{29}$$

and the coefficients of the field inside the particle:

$$\begin{aligned} c_n &= \frac{\mu_1 j_n(x)[x h_n^{(1)}(x)]' - \mu_1 h_n^{(1)}(x)[x j_n(x)]'}{\mu_1 j_n(mx)[x h_n^{(1)}(x)]' - \mu h_n^{(1)}(x)[mx j_n(mx)]'}, \\ d_n &= \frac{\mu_1 m j_n(x)[x h_n^{(1)}(x)]' - \mu_1 m h_n^{(1)}(x)[x j_n(x)]'}{\mu m^2 j_n(mx)[x h_n^{(1)}(x)]' - \mu_1 h_n^{(1)}(x)[mx j_n(mx)]'}. \end{aligned} \tag{30}$$

Here, $m = \frac{k_1}{k} = \frac{N_1}{N}$ is the relative refractive index, and $x = ka = \frac{2\pi N a}{\lambda}$ is the size parameter.

From equations 29 and 30, one can see that the denominators of c_n and b_n are identical to those of a_n and d_n. We say that the a_n mode is dominant when the denominator of a_n is approximately zero, i.e., when the condition:

$$\frac{[x h_n^{(1)}(x)]'}{h_n^{(1)}(x)} = \frac{\mu_1 [mx j_n(mx)]'}{\mu m^2 j_n(mx)} \tag{31}$$

is approximately satisfied [27]. Likewise, the b_n mode is dominant when the condition:

$$\frac{[x h_n^{(1)}(x)]'}{h_n^{(1)}(x)} = \frac{\mu [mx j_n(mx)]'}{\mu_1 m^2 j_n(mx)} \tag{32}$$

is approximately satisfied. The eigenfrequencies are the frequencies that exactly satisfy equations 31 and 32.

The eigenfrequency corresponds to a frequency at which the system has a surface mode. The eigenfrequencies of the one-pillar and two-pillar systems can be used to interpret the hopping amplitude between two sites in the Bose-Hubbard Hamiltonian for the three-site model in the following way. For one pillar, we have an eigenfrequency ω_0. With two pillars, the two isolated modes couple with some coupling term ω. Now we can express the Hamiltonian in the two-pillar basis as

$$H = \begin{pmatrix} \omega_0 & \omega \\ \omega & \omega_0 \end{pmatrix}$$

This Hamiltonian has eigenvalues $\epsilon = \omega_0 \pm \omega$. Therefore, knowing the eigenfrequencies of the systems, we can extract the coupling term ω, which is equivalent to the hopping term t_{AC} in the Bose-Hubbard Hamiltonian.

4 Computational methods

4.1 Eigenfrequency analysis

In this work, optical modes of dielectric pillar structures were investigated using eigenfrequency analysis within the COMSOL Multiphysics[1] Wave Optics Module. This analysis involves solving Maxwell's equations as an eigenvalue problem in the absence of external sources, obtaining the natural electromagnetic modes of the system and their corresponding complex eigenfrequencies. The method is based on the finite element method (FEM), a well-established numerical technique to approximate solutions to partial differential equations in complex geometries and heterogeneous media [28]. In photonics, FEM-based eigenmode analysis is a standard approach to identify resonance conditions in nanostructures, such as Mie-type scatterers and microcavities [29][30].

The governing wave equation in the frequency domain can be written as:

$$\nabla \times \left(\frac{1}{\mu_r} \nabla \times \mathbf{E} \right) - k_0^2 \left(\epsilon_r - \frac{i\sigma}{\omega \epsilon_0} \right) \mathbf{E} = 0, \tag{33}$$

where $\mathbf{E}$ is the electric field, μ_r and ϵ_r are the relative permeability and permittivity, respectively, σ is the electrical conductivity, and $k_0 = \omega/c$ is the free-space wavenumber. In the absence of losses ($\sigma = 0$), the equation describes lossless propagation, while a nonzero σ introduces dissipation. COMSOL implements this equation and solves it using adaptive FEM mesh refinement in the simulation domain.

The dielectric resonators studied consist of cylindrical pillars with radius $R = 150$ nm and refractive index $n = 3$, embedded in air. These dimensions were chosen so that the half-wavelength of the confined mode is on the order of the pillar diameter, enabling strong field localization. To emulate an open system, perfectly matched layers (PMLs) are used to absorb outgoing radiation and prevent artificial reflections at the boundaries. The use of PMLs ensures that the simulated modes correspond to physical quasinormal modes, which decay to the far field and are characterized by complex eigenfrequencies $\tilde{\omega} = \omega_r + i\omega_i$.

The real part ω_r determines the resonant frequency of the mode, while the imaginary part ω_i corresponds to its damping rate. The latter accounts for all energy losses, including material absorption and radiative leakage. The presence of a nonzero ω_i signifies that the mode is leaky: energy escapes the resonator over time. This is typical for finite-sized dielectric resonators in air, where no complete bandgap prevents radiation. The eigenmodes observed are, therefore, quasibound and resemble Mie-type modes. Their electric fields are primarily confined within the high-index pillar but exhibit evanescent tails and far-field radiation patterns beyond the pillar boundary.

We first simulate a single dielectric pillar to determine its fundamental eigenfrequency ω_0 and field distribution. This frequency serves as the on-site energy in the Stub lattice Hamiltonian.

Next, we study a system of two identical pillars separated by a center-to-center distance variable in the range 50–500 nm. These simulations allow us to analyze the

[1]COMSOL Multiphysics® v. 6.3. www.comsol.com. COMSOL AB, Stockholm, Sweden.

coupling between localized modes on adjacent resonators. When the two pillars are close enough to interact, the single-pillar resonance ω_0 splits into two new eigenfrequencies, ω_1 and ω_2, corresponding to hybridized symmetric and antisymmetric modes. The symmetric mode typically exhibits in-phase field oscillations in both pillars, while the antisymmetric mode features a π phase difference.

The frequency difference between single- and two-pillar eigenmodes quantifies the optical coupling between the pillars and serves as the hopping parameter in the effective Stub lattice Hamiltonian as explained in Section 3.5. By varying the pillar separation in COMSOL and tracking the resulting eigenfrequencies, we extract the coupling term as a function of distance. This methodology is commonly used in the design of coupled resonator optical waveguides and photonic molecule systems [31].

An additional advantage of the eigenfrequency formulation is that it provides direct access to the quality factor Q of each mode, defined by:

$$Q = \frac{\omega_r}{2|\omega_i|}. \tag{34}$$

The quality factor measures the ratio of stored energy to energy lost per optical cycle. High Q values indicate long photon lifetimes and low radiative loss. In our case, the simulated pillars exhibit moderate Q values, as expected for high-index dielectric resonators in an air background without full photonic bandgap protection.

Accurate modeling of open optical systems requires careful boundary treatment. PMLs act as artificial absorbing layers that simulate an infinite domain by smoothly damping outgoing waves without reflection. Without PMLs, reflections at simulation boundaries can create artificial standing waves or trap radiation, leading to overestimated Q values and distorted field profiles. In our simulations, PML regions are included on all sides of the computational domain. The absorption profile and thickness are tuned to ensure negligible back-reflection and stable computation of both ω_r and ω_i. This guarantees that the calculated Q-factors reflect only the physical properties of the resonators, not numerical artifacts from the boundary setup.

4.2 Quantum Simulation

Next, we describe the simulation of a three-site bosonic lattice under both closed- and open-system dynamics. The system is modeled with the Bose-Hubbard Hamiltonian in Fock space. We employ the QuSpin[2] library to construct the Hilbert space, build the Hamiltonian matrix, and perform time evolution. In the closed case, the particle number is conserved, and we solve the dynamics via exact diagonalization of the Hamiltonian. In the open case, we include a decay channel at the output site and evolve the density matrix of the system using the Lindblad master equation. Finally, we outline how the switching time is extracted as a function of the inter-site hopping amplitude t_{AC} by analyzing oscillation frequencies in the occupation dynamics.

[2]https://github.com/QuSpin/QuSpin

Closed-System Dynamics: Exact Diagonalization Method

We work in the Fock basis of bosonic occupation number states $|n_A, n_B, n_C\rangle$ with a fixed total number of photons N_b. The Hilbert space is truncated so that $n_i \leq N_{b,\max}$ for each site (here $N_{b,\max} = N_b$ in the closed system, since the total N_b is conserved). The basis states thus satisfy $n_A + n_B + n_C = N_b$. For example, with $N_b = 2$ photons, the basis states include $|2, 0, 0\rangle$, $|1, 1, 0\rangle$, $|1, 0, 1\rangle$, $|0, 2, 0\rangle$, etc., appropriately symmetrized for photons. The dimension of this truncated Fock space grows combinatorially:

$$D = \frac{(N_b + N_{\text{sites}} - 1)!}{N_b!\,(N_{\text{sites}} - 1)!}. \tag{35}$$

In our simulations N_b is small (max. 2), so D remains tractable.

We used the QuSpin package to generate the bosonic Hilbert space and Hamiltonian matrix. QuSpin's `boson_basis_1d` class efficiently constructs the Fock basis of the D states by enumerating all combinations of occupation numbers consistent with N_b. The Hamiltonian operator $\hat{H}$ is then built in this basis by specifying the terms in Eq. 3. In practice, we provide QuSpin with lists of matrix elements for each type of term: hopping terms of the form $\hat{a}^\dagger \hat{c}$, on-site number terms $\hat{n}_i$, and interaction terms $\hat{n}_i(\hat{n}_i - 1)$. QuSpin internally assembles these into the full Hamiltonian matrix $\hat{H}$.

The initial state $|\psi(0)\rangle$ is prepared either as an edge-site Fock state or an *edge-state* superposition. In an edge-site initial state, all N_b photons are placed on the input site A, so $|\psi(0)\rangle = |N_b, 0, 0\rangle$. In an edge-state initial state, we form a coherent superposition localized on the edge: for example, a state localized on the left unit cell can be taken as a superposition of photons on sites A and B with a certain amplitude ratio. These initial states are normalized and represented as vectors in the Fock basis. In this work, we use the edge-site initial state.

With the Hamiltonian matrix H and the initial state $|\psi(0)\rangle$ defined, we determine the eigenvalues and eigenvectors by diagonalizing the Hamiltonian.

$$H = UDU^\dagger \tag{36}$$

where U is a unitary matrix and D is a diagonal matrix. The way to solve these eigenvalue problems is exact diagonalization, which can be divided into exact (LU decomposition) and iterative methods [32]. In practice, QuSpin uses Lanczos diagonalization routines to find eigenvalues E_α and a unitary matrix U of eigenvectors, then computes the matrix exponential $Ue^{-iDt}U^{-1}$ (where $D = \text{diag}(E_\alpha)$) to propagate the state. Lanczos algorithm works well in this problem due to a small Hilbert space, but the computation time does not scale well, increasing at a rate of $O(n^3)$ [33].

We compute the complete set of eigenvalues E_α and eigenvectors $|\phi_\alpha\rangle$ that satisfy $H|\phi_\alpha\rangle = E_\alpha|\phi_\alpha\rangle$. The time evolution can then be written in the eigenbasis as

$$|\psi(t)\rangle = \sum_\alpha e^{-iE_\alpha t}\ \langle\phi_\alpha|\psi(0)\rangle\ |\phi_\alpha\rangle\ . \tag{37}$$

which is equivalent to $|\psi(t)\rangle = e^{-iHt}|\psi(0)\rangle$. QuSpin offers a direct ODE solver for time evolution; in fact, we utilize its `hamiltonian.evolve` method to compute

$|\psi(t)\rangle$ on a time grid t_n without having to manually exponentiate the matrix. Both approaches yield the exact unitary evolution for this closed quantum system.

To analyze the results, we calculate expectation values of observables as functions of time. The primary observables of interest are the site occupation numbers $\hat{n}_i = b_i^\dagger b_i$. We compute $\langle n_m(t)\rangle$ efficiently using QuSpin by constructing the number operator $\hat{n}_m$ as a matrix and evaluating $\langle\psi(t)|\hat{n}_m|\psi(t)\rangle$ at each time t_n. The result is a set of time series $n_A(t), n_B(t), n_C(t)$ that track how particles redistribute among the sites. Other quantities, such as energy $E(t) = \langle\psi(t)|H|\psi(t)\rangle$, can be obtained similarly by constructing the appropriate operators.

Open-System Dynamics: Density matrix

To investigate the effects of dissipation, we introduce a single-particle loss channel at the output site, which acts as a sink for photons. Physically, this can represent coupling of site C to an external reservoir or absorption by a dissipative waveguide.

We simulate Lindblad dynamics by evolving $\hat{\rho}(t)$ directly. The Hilbert space basis must accommodate varying particle number up to $N_{b,\max}$ (the initial number), since over time the system can occupy states with $N_{b-1}, N_{b-2}, \ldots$ photons after losses. To achieve this, we construct a bosonic Fock basis that includes all states from 0 to $N_{b,\max}$ total photons. This is done in QuSpin by specifying a list of allowed total particle numbers when initializing the basis. The size of the basis thus grows compared to the closed case (for example, including up to $N_{b,\max} = 5$ photons at three sites yields $D = \frac{(5+2)!}{5!,2!} = 21$ states for exactly 5 photons, plus additional states for fewer photons, for a total of $1 + 3 + 6 + 10 + 15 + 21 = 56$ basis states). The Hamiltonian H is constructed in this extended basis in the same way as before, but H now acts within a subspace of indefinite particle number. We then solve Eq. 21 as a first-order ODE for the density matrix.

For numerical efficiency, we vectorize the density matrix and implement the master equation as $\dot{\hat{\rho}} = \mathcal{L}(\rho)$, where $\mathcal{L}$ is the Lindbladian super-operator. QuSpin's ODE integrator (from quspin.tools.evolution) is used to step this equation in time. We compute $\hat{L}(\rho)$ at each step, and subsequently the ODE solver outputs $\rho(t_n)$ at each time point t_n in our simulation grid.

From the density matrix, we compute the observables as trace expectations. In the simulation, after obtaining $\rho(t_n)$, we evaluate $\langle n_m(t_n)\rangle = \mathrm{Tr}[\rho(t_n), N_m]$ for each site m, where N_m is the matrix representation of $\hat{n}_m$. The result is again a set of time series $n_A(t), n_B(t), n_C(t)$, now reflecting open-system behavior. In the open system, $n_C(t)$ will typically decay toward zero at long times due to the loss, and the total $\langle n_A\rangle + \langle n_B\rangle + \langle n_C\rangle$ also decays as photons are removed from the system.

Switching Time

A central quantity of interest is the switching time t_{switch}, which we define as the characteristic time for the system to switch from the "OFF" state to the "ON" state. In our three-site model, an effective way to quantify this switching is to examine the oscillatory transfer of population from the input to the output site. When the switch

is activated, the populations $n_A(t)$ and $n_C(t)$ will exhibit oscillations as the photons tunnel back and forth. We extract t_{switch} by analyzing the frequency content of these oscillations.

In practice, after running the time evolution for a given set of parameters, we perform a Fourier transform of the time-dependent occupancy signals. The Fourier spectrum typically exhibits a peak at a dominant oscillation frequency ω_{peak}. This frequency corresponds to the Rabi oscillation induced by the coupling t_{AC}. We identify ω_{peak} using a peak-finding algorithm in the Fourier magnitude spectrum. The switching time in closed dynamics is then related to this frequency by

$$t_{\text{switch}} \approx \frac{\pi}{\omega_{\text{peak}}}, \tag{38}$$

i.e., essentially a half-period of the dominant oscillation. This definition is consistent with the intuitive notion that a faster oscillation (higher ω_{peak}) implies a shorter time to transfer population to the output, and thus a faster switch. One should note that in open dynamics, the switching time is defined as a sufficient probability that the photon has been depleted through the decay channel. Thus, the switching time depends on the time scale introduced by the decay rate in addition to the Rabi oscillation time scale.

To study how t_{switch} depends on the lattice parameters, we repeated the simulations for various values of the hopping amplitude t_{AC} (keeping the other parameters fixed) and extracted the switching time for each case. By plotting t_{switch} versus t_{AC}, we obtain a switching time curve from which an optimal range can be identified.

5 Results

In this section, we present the main results of this thesis: the eigenmodes and frequencies of the dielectric pillars and the quantum behavior of photons in a three-site model. We start by introducing the data from quantum simulations, concentrating on the switching time as a function of hopping amplitude. After that, we show the results of the eigenfrequency analysis. We present the hopping amplitude as a function of the distance between the pillars and show the optical modes that lead to the optimal switching time.

5.1 Closed dynamics

To quantify the switching performance, we examine the switching time t_{switch}, defined in the closed system as the half-period of the Rabi oscillation required to transfer the photon pair from input to output. We first investigate how the coupling ratio r_{AB} affects the behavior of the switch. The probability of detecting single- or two-photon events at the output sites at time t_{switch} is presented in Fig. 5a. For small r_{AB}, we observe a significant "OFF" state leakage; a single photon initially at A was not perfectly confined, thus leaking partially into the output sites. By increasing $|r_{\text{AB}}|$, we increase the energy gap $|E_{\pm} - E_{\text{loc}}|$ and concentrate the $E = 0$ mode's weight more on the input site A, thus suppressing single-photon tunneling. Our simulations show that the "OFF" state leakage probability decreases substantially as $|r_{\text{AB}}|$ increases. However, this comes at the cost of a longer switching time, as can be seen in Fig. 5b. We found that t_{switch} increases steeply with $|r_{\text{AB}}|$ for large ratios.

This trade-off can be understood from the eigenmode picture. A larger coupling imbalance $|r_{\text{AB}}|$ pushes the dispersive mode energies $E_{\pm}$, in Eq. 8, further from the flat band, reducing resonant mixing between localized and two-photon delocalized states. In the perturbative view, when the energy detuning is large compared to the interaction-induced coupling, the Rabi frequency (and hence switching speed) is reduced. Thus, increasing $|r_{\text{AB}}|$ improves the contrast between the "OFF" and "ON" states (by isolating the localized mode) but also slows down the switch. We chose an intermediate value, $r_{\text{AB}} = -4$, as an optimal compromise that keeps the OFF-state leakage low while limiting the slowdown of the switching dynamics.

Subsequently, we investigated how the switching time varies with the magnitude of the hopping strength t_{AC} (with $r_{\text{AB}} = -4$). The theory developed in Section 3.3 predicts that the two-photon oscillation frequency, and hence t_{switch}, is governed by the interplay of t_{AC} and U. In particular, for very weak hopping ($t_{\text{AC}} \ll U$), the photons are localized for a long time. In the opposite strong hopping limit ($t_{\text{AC}} \gg U$), the flat-band condition is lost, a single photon is only partially localized, so the distinction between "OFF" and "ON" states blurs, and the effective two-photon coupling is again reduced.

Consequently, there exists an optimal intermediate coupling that maximizes the two-photon transfer rate. Our numerical results, presented in Fig. 6, reveal a minimal switching time at a finite hopping amplitude: specifically around $t_{\text{AC}} \approx 0.29U$. At this optimal point, the interaction shifts the two-photon energy just enough to match

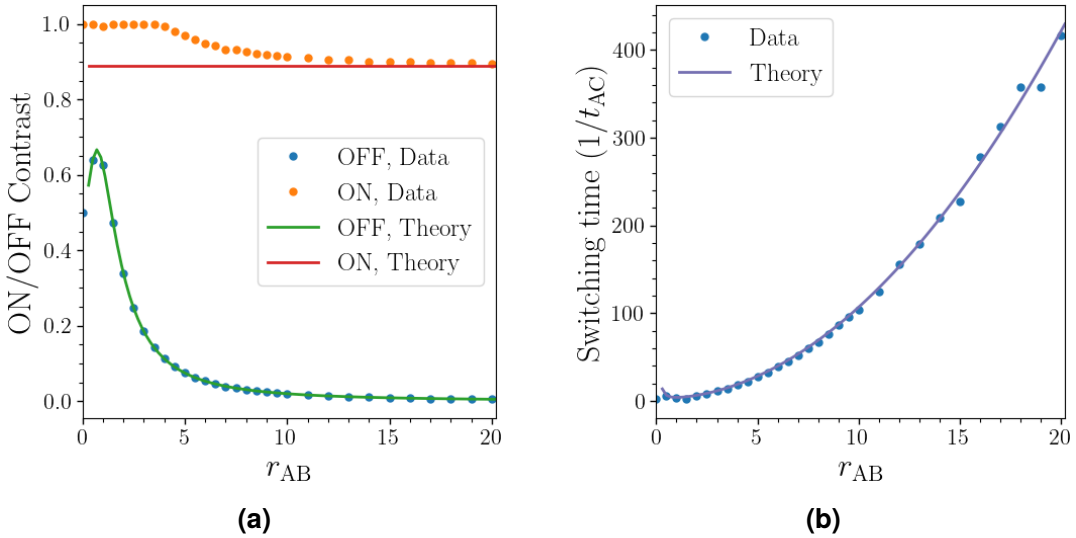

Figure 5: The switching concept in a closed operation at $U = t_{AC}$. **(a)** Dependence of the output-site photon occupancy in the "ON" and "OFF" states on the coupling ratio r_{AB}. **(b)** The switching time as a function of r_{AB}.

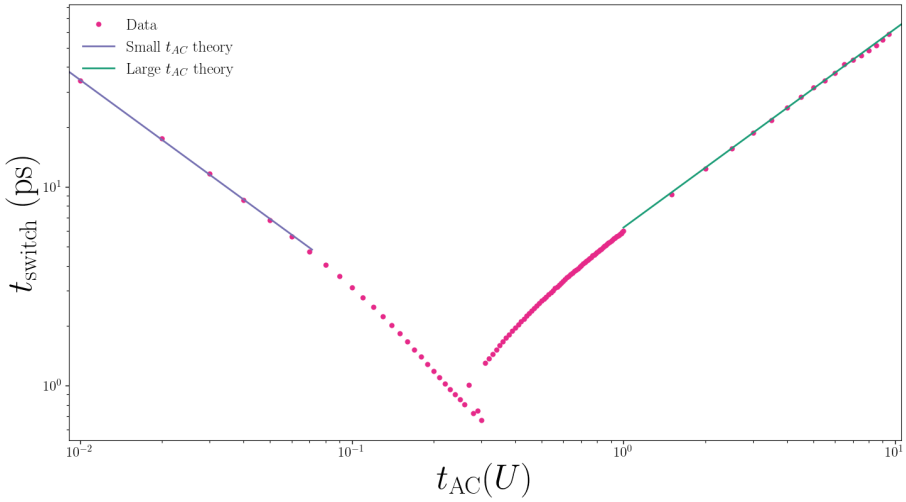

Figure 6: Switching time as a function of hopping term in the Stub lattice in closed dynamics.

the gap between the bands, which results in the fastest possible Rabi oscillation. The simulated switching time here is $t_{switch,min} \approx 0.72$ ps, which is extremely fast on optical timescales. In particular, the data points align well with the theoretical lines obtained from our two-level model in the limits of small and large t_{AC}, which confirms the validity of the Rabi oscillation picture.

Finally, we examine the dynamics of the system with the optimal parameters, $t_{AC} = 0.29U$ and $r_{AB} = -4$, to confirm the switching mechanism. Figures 7a and 7b (upper panel) show that with two photons initially at site A, the probability of detecting both photons at the output sites oscillates sinusoidally over time. However, there is a

clear distortion on top, suggesting that the dynamics is influenced by more than just a simple two-level transition.

Meanwhile, a single photon at A remains trapped: as shown in the lower panels of Figures 7a and 7b, the probability of a single photon leaving the input is close to zero, aside from a small oscillatory leakage of the order of 0.1–0.2. This residual leakage reflects the fact that our initial single-photon state is not exactly the ideal localized eigenstate. The leakage oscillates in time but never exceeds 20%, indicating that most of the single-photon amplitude stays confined at A. If even a lower leakage is desired, $|r_{\mathrm{AB}}|$ could be further increased, at the expense of a longer switching time, as noted above.

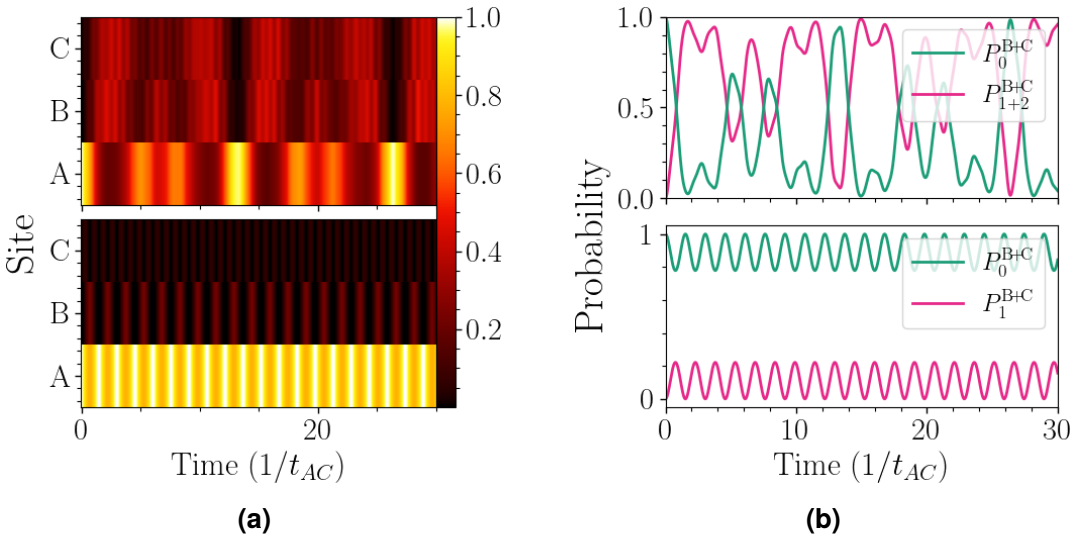

Figure 7: The switching concept in a closed operation at $t_{\mathrm{AC}} = 0.29U$ and $r_{\mathrm{AB}} = -4$. **(a)** The normalized particle number at different sites as a function of time.**(b)** The probability to detect $n = \{0, 1, 2\}$ photons at the output sites as a function of time.

We note that this three-site Stub switch, being the minimal flat-band unit, inherently has some finite OFF-state leakage. This is a known limitation compared to larger flat-band lattices such as the diamond chain (an Aharonov–Bohm cage) where single-photon localization can be perfect [4]. In the diamond chain, destructive interference can confine a single photon completely with zero tunneling, yielding ideally an infinite ON/OFF contrast. However, the advantage of a Stub lattice is its simplicity. It requires only three sites and no magnetic flux or additional phase engineering, which could be easier to implement in photonic hardware.

5.2 Open dynamics

As in the closed system, increasing the coupling ratio $|r_{\mathrm{AB}}|$ improves the isolation of the single-photon localized state. In Figures 8a and 8b one can see the switching contrast and the switching time as a function of r_{AB}. The results show that both the "OFF" state leakage and the two-photon throughput are sensitive to r_{AB}. One can see

that t_{switch} in the open regime also grows with $|r_{\text{AB}}|$, similar to the closed case. We again choose $|r_{\text{AB}}| = 4$ as a reasonable trade-off that gives us a high ON/OFF contrast while keeping the switching time within acceptable limits.

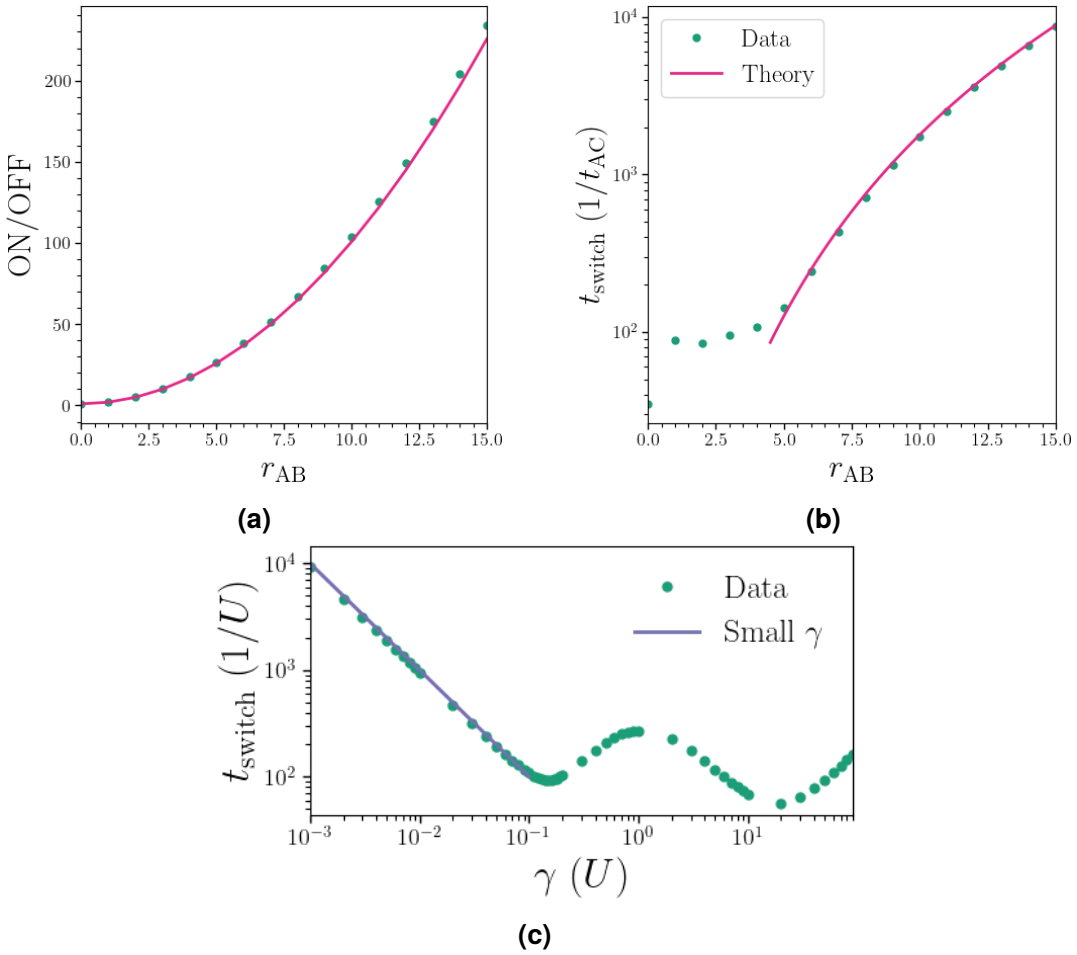

Figure 8: The switching concept in an open operation at $t_{\text{AC}} = U$. **(a)** Dependence of the "ON" versus "OFF" signal contrast on r_{AB}. **(b)** The switching time as a function of r_{AB}. **(c)** The switching time as a function of decay rate γ.

In open dynamics, there is an additional parameter, decay rate γ, to optimize. In Fig. 8c, the switching time can be seen as a function of γ. If γ is too low, the photons will linger in the lattice and may Rabi oscillate back to the input before being lost, reducing the switching contrast and increasing the time to fully remove them. On the other hand, if γ is too high, it can overdamp the dynamics, the moment one photon of the pair reaches C, it becomes absorbed so rapidly that its partner might remain behind (breaking the correlated pair transport) or the overall probability of two-photon transmission might drop. Fig. 8c presents the dependency of t_{switch} on the decay rate γ. One can see that the switching time has the first minimum at $\gamma \approx 0.1 t_{\text{AC}}$ value. We fix γ at this value for subsequent measurements.

With r_{AB} and γ optimized, we examine the switching time as a function of t_{AC}, presented in Fig. 9. Remarkably, we found a very similar behavior to the

closed case: t_{switch} is minimized at roughly $t_{\text{AC}} \approx 0.29U$, the same optimal range as before. However, the minimum switching time achieved in the open configuration is significantly longer than in the closed case; on the order of tens of picoseconds in our simulations ($t_{\text{switch,min}} \approx 26$ ps at $t_{\text{AC}} \sim 0.29U$). This slowdown is expected, as the limiting factor is now in part the dissipative time scale $1/\gamma$ in addition to the Rabi oscillation timescale. In a closed system, the speed is limited by how fast coherent hopping plus interaction can redistribute the photons. In the open system, even after the photons reach the output site, one must wait for them to be absorbed; the overall switching event cannot be faster than a few times $1/\gamma$. In our case $\gamma = 0.1$U. This introduces an additional slowing factor. More formally, the analysis of the Lindblad master equation in Section 3.4 indicates that t_{switch} in the presence of loss is governed by the damped Rabi oscillation frequency and the combined loss rate. Our data show that beyond the optimum, if t_{AC} is further increased, the switching time starts to increase again, mirroring the closed system behavior. Thus, even with dissipation, there is an optimal coupling that balances speed and localization.

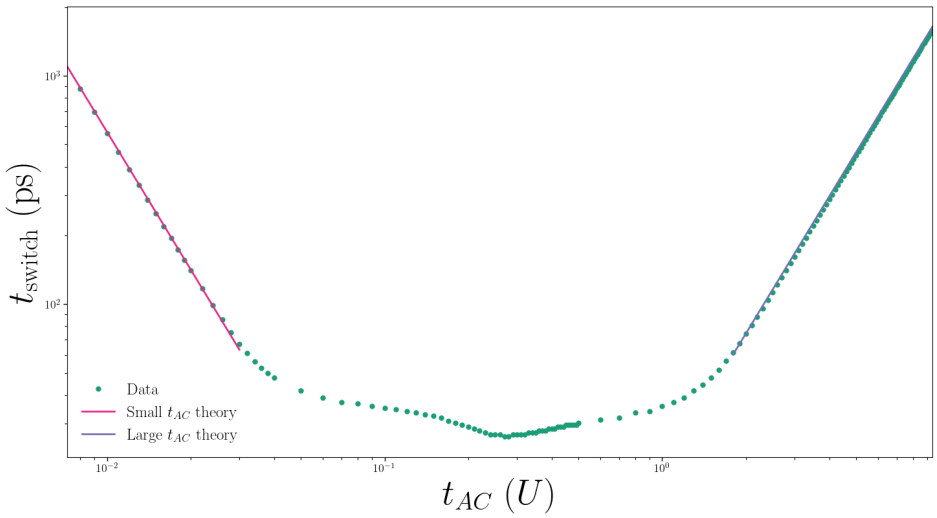

Figure 9: Switching time as a function of hopping term in the Stub lattice in open dynamics.

The dynamics of the open switch provides additional insight. In the upper panels of Figures 10a and 10b, we plot the normalized populations of each site as a function of time for the two-photon initial state. At $t = 0$, both photons are at site A. As time progresses, one can see the population oscillating to site C and then being permanently removed. The two-photon population at A correspondingly decreases close to zero after one oscillation cycle, indicating that the pair has successfully left the input.

Meanwhile, the lower panels of Figures 10a and 10b show the single-photon case: a lone photon initially at A remains almost entirely localized at A for all times, with its probability at the output sites staying close to zero except for tiny oscillations. Over long times, the single-photon probability at A tends to a finite value (a plateau), meaning that a portion of the photon's amplitude never decays. Any small probability that does leak to C is quickly lost, so the net transmission of a single photon is virtually

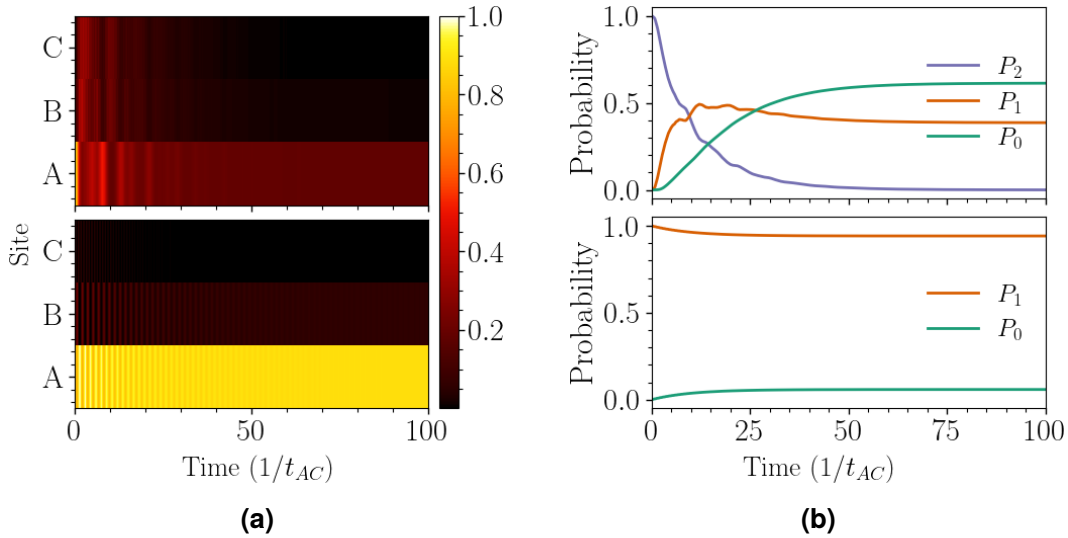

(a) **(b)**

Figure 10: **(a)** Normalized particle number dynamics at each site, starting from two (upper panel) and a single (lower panel) photons initially at site A. **(b)** The probability to detect $n = \{0, 1, 2\}$ photons at the output sites as a function of time. The parameters are $\gamma = 0.1t_{\mathrm{AC}}$, $r_{\mathrm{AB}} = -4$ and $t_{\mathrm{AC}} = 0.29U$.

zero.

5.3 Eigenfrequencies

Subsequently, we aim to find the optimal distance between the pillars for a minimal switching time. So far, our results have been expressed in terms of the dimensionless Bose–Hubbard parameters (t_{AC}, U, etc.). To bridge these findings with a real photonic implementation, we performed a 2D eigenfrequency analysis using COMSOL for a system of dielectric micropillars that emulates the Stub lattice sites. The goal is to identify a practical geometry (pillar size, refractive index, and spacing) that realizes the required hopping amplitude for optimal switching, and to ensure that the operating optical modes are well behaved (e.g. reasonably high Q factor and distinct from other modes).

In our design, each lattice site is a 2D resonator (pillar) supporting a confined optical mode. Tunneling between sites occurs through the evanescent coupling of these modes when the pillars are placed in proximity. By adjusting the center-to-center distance between the pillars, one can tune the overlap of their evanescent fields and hence the hopping rate t_{AC}. We focus on the fundamental transverse mode of an isolated pillar, which in our simulation appears at a complex eigenfrequency $\omega \approx 400.71 + 4.79i$ THz for a pillar with a radius of 150 nm, as can be seen in Fig. 12a. The quality factor of this single-pillar mode is calculated as $Q = \omega_r/(2\omega_i) \approx 41.8$, which is relatively modest, implying that in a standalone pillar the photon decays after on the order of $Q/(2\pi) \sim 6 - 7$ optical cycles. For our switching purposes, $Q \sim 40$ may not be enough: a photon with a frequency of 400 THz has a period of 2.5 fs, so a $Q = 40$ mode decays in roughly $6 \cdot 2.5\mathrm{fs} \approx 15$ fs. This is much shorter than our switching

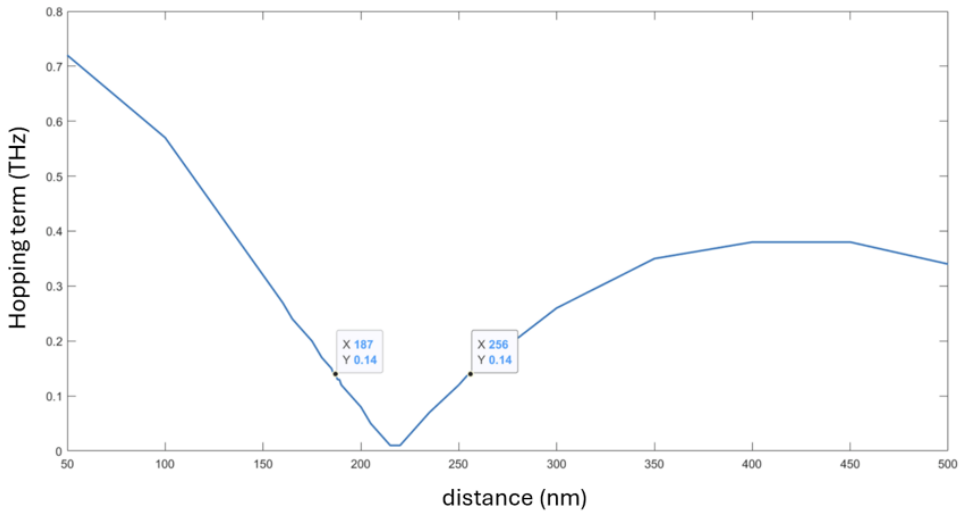

Figure 11: Hopping term as a function of distance between the pillars.

times (~ps or more), but it could potentially be improved by using a photonic crystal slab to confine the mode.

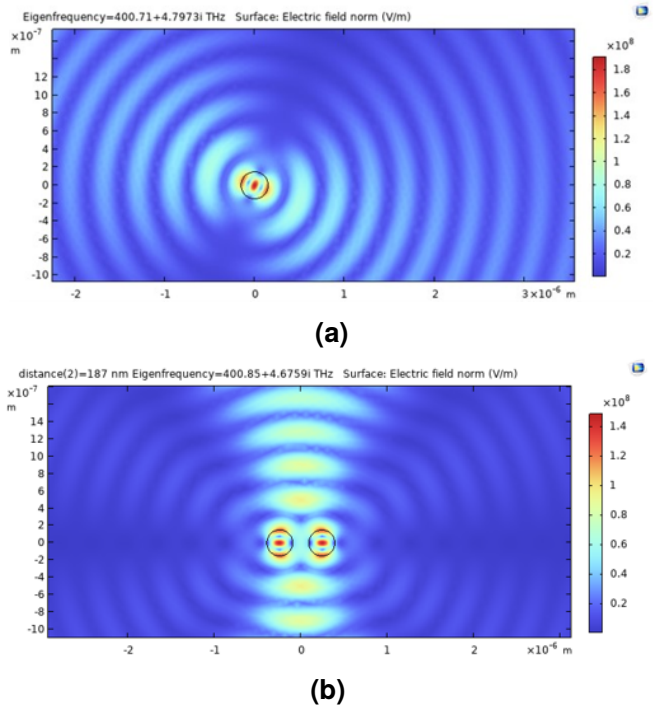

(a)

(b)

Figure 12: Surface electric field norms of optical eigenmodes in single- and two-pillar systems. **a)** Eigenfrequency analysis of a single pillar reveals the on-site energy, indicated in the top-left corner. **b)** An inter-pillar separation of 187 nm is chosen to match the optimal hopping amplitude.

From these simulations, we could calibrate t_{AC} in physical units. The hopping energy t_{AC} corresponds to the eigenfrequency difference between the one- and

two-pillar modes, as explained in Section 3.5. For a realistic Kerr nonlinearity of $n_2 \sim 10^{-9}$ m^2/W (as reported in GaAs/AlGaAs multiple quantum wells), and assuming a mode volume on the order of one cubic wavelength, one can achieve an interaction energy on the order of $U \sim 2 \cdot 10^{-3}$ eV [34][4]. The optimal hopping is then $t_{\mathrm{AC}} \approx 0.29U \approx 5.6 \times 10^{-4}$ eV. In frequency units, this is $t_{\mathrm{AC}}/h \approx 0.14$ THz. Our two-pillar eigenmode calculations show that this target hopping frequency can be obtained at sub-micrometer pillar spacings. Fig. 11 presents the hopping amplitude in units [Hz] as a function of the distance between the pillars. The distances of 187 nm and 256 nm yield the eigenfrequency difference corresponding to $t_{\mathrm{AC}} \approx 0.14$ THz. Therefore, we identify $\sim 0.19\mu$m and $\sim 0.26\mu$m as optimal distances for our chosen pillar parameters, which perform the fastest switching according to our model. To visualize the coupled mode at distance 187 nm, Fig. 12b shows the electric field profile of the symmetric two-pillar resonance at $d = 187$ nm. This mode has a complex frequency $400.85 + 4.68i$THz, very close to the single pillar frequency. The quality factor of the symmetric mode is calculated as $Q \approx 42.9$, essentially unchanged from the isolated pillar, meaning that the introduction of a neighbor does not incur additional radiative losses. We can thus conclude that our quantum model parameters are realizable with current photonic materials and structures, but there is a need for improvement in the confinement of the mode.

6 Discussion

In this thesis, we have investigated a novel all-optical switching mechanism based on flat-band-induced localization in a three-site Stub lattice. Using the Bose–Hubbard model, we analyzed how destructive interference in a flat band can localize a single-photon state (the "OFF" state) and how the introduction of a second photon with weak on-site interaction leads to interaction-induced delocalization (the "ON" state). We studied both closed system (particle-conserving) dynamics and open system dynamics (with a loss channel), and confirmed that in the closed operation the two photons undergo Rabi oscillations between the input and output sites while a single photon remains trapped, while in the open operation the decay rate γ dampens the oscillations until the system is depleted. A key theoretical result is that the performance of the switch, quantified by the switching time required to transition from the "OFF" state to the "ON" state, can be optimized by tuning the lattice parameters. In particular, we found that there is an optimal inter-site coupling that minimizes the switching time. Too weak coupling retains the photon localization for too long, whereas too strong coupling undermines the flat-band interference condition.

By simulating realistic photonic pillar parameters, we identified the coupling that balances speed and localization, yielding the shortest switching time for a given interaction strength. These simulations demonstrated ultrafast switching dynamics; < 1 ps for the closed dynamics and ≈ 26 ps for the open dynamics. This highlights the promise of flat band systems for achieving ultrafast optical switching at the single-photon level.

Conventional all-optical switches (such as those based on nonlinear Mach–Zehnder interferometers or cavity resonance shifts) typically rely on the optical Kerr effect or similar nonlinearities to accumulate a phase shift or bistable response, often requiring intense control pulses or many photons to achieve switching [1][5]. For example, in a nonlinear Mach–Zehnder interferometer (MZI) switch, a high-intensity control beam induces a refractive index change that causes destructive interference of the signal in one arm when the control is "ON". However, at the few-photon limit, MZI-based switches face fundamental challenges: coherent light, intensity fluctuations, and the limited phase shift per photon make reliable operation impractical [4].

Even using Fock-state control photons, one estimates that extremely long interaction lengths (on the order of millimeters in GaAs-based waveguides) would be required to accumulate a π phase difference with a single photon, far beyond what is feasible on chip [4]. In contrast, the flat-band switch exploits interference localization: the control photon does not need to impart a π phase shift to the entire system, but instead any small nonlinearity can break the delicate cancellation of amplitudes that generates the localized flat-band state. This distinction means that even very weak nonlinearities (far below those required for MZI switching) can, in principle, achieve switching, although with a longer delay if the nonlinearity is extremely weak [4].

Importantly, our concept operates with single photons as both signal and control, reaching the fundamental quantum limit of switching. We note that in our three-site Stub lattice model the OFF-state leakage is not strictly zero; a small probability of single-photon escape exists due to the finite lattice size. However, this leakage can be

minimized by lattice design (increasing the ratio r_{AB}), and in larger flat band lattices such as the diamond chain, an ideal infinite suppression of single-photon transport is theoretically achievable [4]. Overall, compared to traditional switching paradigms, the flat-band switch offers a fundamentally different route: it achieves switching with ultra-low control energy and uses interference engineering to amplify the effect of modest nonlinear interactions.

The primary advantage of the flat band all-optical switch is its operation in the single photon limit, thus achieving the minimal possible switching energy. This enables for an all-optical transistor-like behavior at the quantum level, which could be transformative for optical computing and quantum information processing. Another benefit is the ultrafast response of the switching mechanism. Because the switching is driven by the intrinsic dynamics of a two-photon delocalization, the timescale can be very short: on the order of $\sim$ 1 ps, as shown in this thesis. This is comparable to the fastest optical switches that have been demonstrated and typically use much higher optical powers [15][4]. Moreover, the flat-band switch does not rely on any exotic medium for nonlinearity beyond a moderate Kerr nonlinearity; it effectively leverages time (photon storage in a trapped state) instead of requiring a large nonlinearity. This means that a wide range of material platforms could be used, and the concept is not tied to a specific wavelength or material as long as interference localization and a nonlinear interaction are present.

However, there are notable limitations. Even though the single-photon limit can be a benefit, it is also a limitation since the flat-band switch presented in this work ceases to function correctly if the signal or control fields contain many photons. In a high-intensity regime, the additional photons would themselves trigger unwanted delocalization or saturate the effect, effectively removing the ON/OFF distinction [4]. This limits the immediate practical use of the concept for classical optical communication, where switches typically need to handle large photon fluxes.

Another limitation is the sensitivity to photon losses and decoherence. The flat band localization relies on coherent interference, so any loss or dephasing in the system can degrade the "OFF" state or disrupt the "ON" state dynamics. The switching time must therefore be shorter than the photon lifetime in the device; achieving picosecond switching is beneficial in this regard, but it demands ultra-low-loss photonic structures in whichever platform is used. The eigenfrequency analysis presented in this work revealed a poor Q factor for the eigenmodes: $Q \sim 40$. This is not enough for an optimally working switch, but the Q factor could potentially be improved by using a photonic crystal slab. However, by this approach, the switch would lose its main benefit of simplicity.

Finally, the need for single-photon control signals means that the switch must interface with single-photon sources and detectors, which, although rapidly advancing, are still challenging to integrate at scale. These considerations mark the flat band switch as a promising but long-term approach, likely to find its first applications in quantum photonics rather than in immediate classical optical switching networks.

This work opens some avenues for further investigation. First, it would be valuable to explore larger flat-band lattices and more complex geometries beyond the minimal three-site cell. For example, the diamond chain was identified in Reference [4] as an

alternative model where the flat-band switch concept yields perfect ON/OFF contrast. Studying a full diamond chain or other flat-band networks (e.g. Lieb lattices or Kagome lattices with flat bands) could reveal whether multiple switching cells can be stacked or if the switching performance can be improved with scale. Another direction is to investigate topologically nontrivial flat bands. These are, for instance, flat bands that arise in lattices with synthetic magnetic flux or spin-orbit coupling, which can host robust edge states. Incorporating topological protection into the flat-band switch might make localization more resistant to fabrication disorders or enable unidirectional switching behavior [19].

One possible extension is to explore methods to trigger the switch with external control in a hybrid manner, for instance, using an external optical or microwave field to dynamically tune the lattice parameters and thereby control the ON/OFF state without needing a second photon. This might bridge the gap between the purely quantum operation of the current design and a more classical control over the switch state. Finally, continued improvements in single-photon sources, detectors, and nonlinear materials will directly benefit the viability of the flat-band switching mechanism. As single-photon technology matures (with higher repetition rates and efficiency), the prospect of a true single-photon-by-single-photon logic device becomes more realistic.

In conclusion, the flat-band all-optical switch studied here provides a conceptual foundation for ultralow-power, ultrafast photonic switching. The method leverages the distinctive physics of flat bands, dispersionless states, and interference localization to overcome some long-standing obstacles in optical switching at the quantum limit. Although practical deployment will require overcoming technological challenges, our results indicate that such switches could eventually be implemented in photonic structures, offering new functionalities for quantum photonics and opening the path toward integrated photonic circuits where light is controlled by light at the single-photon level. The insights gained from this work suggest that interference-engineered lattices are a promising route forward, and we anticipate that further theoretical and experimental efforts will expand the boundaries of flat-band-based photonics in the years to come.

Appendix A. Derivation of the Stub lattice eigenstates

According to Bloch's theorem, the eigenstates in a periodic lattice can be expressed as $\psi_k(r) = e^{-ikr}u(r)$, where $u(r)$ is a periodic function: $u(r) = u(r+a)$. Similarly, creation and annihilation operators can be defined in momentum space using Fourier transforms:

$$\hat{a}_j = \sum_k e^{ikR_j}\hat{d}_k,\ \hat{b}_i = \sum_k e^{ikR_j}\hat{e}_k \text{ and } \hat{c}_j = \sum_k e^{ikR_j}\hat{f}_k.$$

Here, $R_j = aj$ denotes the position of the jth unit cell, where a is the lattice spacing. The momentum space is defined over the periodic interval $k \in [-\frac{\pi}{a}, \frac{\pi}{a}]$, corresponding to the first Brillouin zone. As an illustration, the hopping term between neighboring sites A_{j+1} and C_j in the real space transforms into the following form:

$$\begin{aligned}\sum_j \hat{a}^\dagger_{j+1}\hat{c}_j &= \sum_j \sum_{k,k'} e^{-i(kR_{j+1}-k'R_j)}\hat{d}^\dagger_k\hat{f}_{k'} = \sum_{k,k'} e^{iak}\overbrace{\sum_j e^{-i(k'-k)aj}}^{\delta_{k',k}}\hat{d}^\dagger_k\hat{f}_{k'} \\ &= \sum_k e^{iak}\hat{d}^\dagger_k\hat{f}_k\end{aligned}$$

Now we perform the Fourier transform to transform the Hamiltonian 3 to momentum space.

$$\begin{aligned}H &= \sum_n \epsilon_A\hat{a}^\dagger_n\hat{a}_n + \epsilon_B\hat{b}^\dagger_n\hat{b}_n + \epsilon_C\hat{c}^\dagger_n\hat{c}_n - t_{AC}(\hat{a}^\dagger_n\hat{c}_n + \hat{a}^\dagger_{n+1}\hat{c}_n + \text{H.c.}) - t_{BC}(\hat{b}^\dagger_n\hat{c}_n + \text{H.c.}) \\ &= \sum_k \epsilon_A\hat{d}^\dagger_k\hat{d}_k + \epsilon_B\hat{e}^\dagger_k\hat{e}_k + \epsilon_C\hat{f}^\dagger_k\hat{f}_k - t_{AC}[(1+e^{ika})\hat{d}^\dagger_k\hat{f}_k + \text{H.c.}] - t_{BC}(\hat{e}^\dagger_k\hat{f}_k + \text{H.c.})\end{aligned} \tag{A.1}$$

This can be written in matrix form:

$$H = \sum_k \begin{pmatrix}\hat{d}_k \\ \hat{e}_k \\ \hat{f}_k\end{pmatrix}^\dagger \begin{pmatrix}\epsilon_A & 0 & -t_{AC}(1+e^{ika}) \\ 0 & \epsilon_B & -t_{BC} \\ -t_{AC}(1+e^{-ika}) & -t_{BC} & \epsilon_C\end{pmatrix}\begin{pmatrix}\hat{d}_k \\ \hat{e}_k \\ \hat{f}_k\end{pmatrix} \tag{A.2}$$

Since we are interested only in the shape of the energy bands, we can simplify by setting $\epsilon_A = \epsilon_B = \epsilon_C = 0$. Thus, we can solve the eigenvalues as follows.

$$-E_k(E_k^2 - t_{BC}^2) - t_{AC}^2E_k(1+e^{ika})(1+e^{-ika}) = 0 \tag{A.3}$$

$$E_k = \begin{cases}-\sqrt{t_{BC}^2 - 2t_{AC}^2(1+\cos(ka))} \\ 0 \\ \sqrt{t_{BC}^2 - 2t_{AC}^2(1+\cos(ka))}.\end{cases} \tag{A.4}$$

The middle eigenenergy $E_k = 0$ is independent of the momentum, indicating a completely flat band with degenerate eigenstates. These can be obtained from the eigenvalue equation $H\,|\psi_k\rangle = E_k\,|\psi_k\rangle$.

$$|\tilde{\psi}_{\mathrm{FL}}\rangle = [\hat{d}_k^\dagger - \frac{t_{\mathrm{AC}}}{t_{\mathrm{BC}}}(1 + e^{ika})\hat{e}_k^\dagger]\,|0\rangle \tag{A.5}$$

Now, we can use an inverse Fourier transform to obtain the flat band states in the position space.

$$\begin{aligned}
|\tilde{\psi}_{\mathrm{FL}}\rangle &= \sum_k [\hat{d}_k^\dagger - \frac{t_{\mathrm{AC}}}{t_{\mathrm{BC}}}(1 + e^{ika})\hat{e}_k^\dagger]\,|0\rangle \\
&= \sum_k \sum_j [e^{-ik(R_j - R_{j'})}\hat{a}_j^\dagger - \frac{t_{\mathrm{AC}}}{t_{\mathrm{BC}}}(1 + e^{ika})e^{-ik(R_j - R_{j'})}\hat{b}_j^\dagger]\,|0\rangle \\
&= \sum_j [\delta_{j',j}\hat{a}_j^\dagger - \frac{t_{\mathrm{AC}}}{t_{\mathrm{BC}}}(\delta_{j',j} + \delta_{j',j-1})\hat{b}_j^\dagger]\,|0\rangle \\
&= [-\frac{t_{\mathrm{AC}}}{t_{\mathrm{BC}}}\hat{b}_{j-1}^\dagger + \hat{a}_j^\dagger - \frac{t_{\mathrm{AC}}}{t_{\mathrm{BC}}}\hat{b}_j^\dagger]\,|0\rangle
\end{aligned} \tag{A.6}$$

We can see that the flat band state is localized at the three sites A_j, B_j, and B_{j-1}. The localization can be concentrated at site A by increasing the ratio $r_{\mathrm{AB}} = \frac{t_{\mathrm{BC}}}{t_{\mathrm{AC}}}$.

Appendix B. Electric field expansion

This proof is based on Ref. [27]. The incident wave expansion E_i in the vector spherical harmonics can be written as

$$E_i = \sum_{m=0}^{\infty}\sum_{n=m}^{\infty}(B_{emn}\mathbf{M}_{emn} + B_{omn}\mathbf{M}_{omn} + A_{emn}\mathbf{N}_{emn} + A_{omn}\mathbf{N}_{omn}) \tag{B.1}$$

Since $\sin(m\phi)$ and $\cos(m'\phi)$ are orthogonal for all values m and m', the functions $\mathbf{M}_{emn}$ and $\mathbf{M}_{omn}$ are likewise orthogonal in the corresponding sense [27]:

$$\int_0^{2\pi}\int_0^{\pi}\mathbf{M}_{em'n'}\mathbf{M}_{omn}\sin\theta d\theta d\phi = 0 \text{ for all } m, m', n, n'. \tag{B.2}$$

Similarly, $(\mathbf{N}_{omn'}, \mathbf{N}_{emn})$, $(\mathbf{M}_{emn'}, \mathbf{N}_{emn})$ and $(\mathbf{M}_o mn')$,$(\mathbf{N}_{omn})$ are mutually orthogonal.

We still need to prove that $(\mathbf{N}_{emn'}, \mathbf{M}_{omn})$ and $(\mathbf{M}_{emn'}, \mathbf{N}_{omn})$ are orthogonal. To interpret this, we must show that the integral:

$$m\int_0^{\pi}\left(P_n^m\frac{dP_{n'}^m}{d\theta} + P_{n'}^m\frac{dP_n^m}{d\theta}\right) = P_n^m P_{n'}^m\Big]_0^{\pi} \tag{B.3}$$

vanishes for all n and n'. Here, P_n^m is the associated Legendre function, which corresponds to the mth derivative of the Legendre polynomial P_n:

$$P_n^m(\cos\theta) = (1-\cos^2\theta)^{m/2}\frac{d^m P_n(\cos\theta)}{d\cos^m\theta}. \tag{B.4}$$

Since $(1-\cos^2\theta) = 0$ for $\theta = \pi$ or $\theta = 0$, it follows that Eq. B.3 vanishes for all m, n, and n'.

To prove the rest of the orthogonality relations,

$$\begin{aligned}\int_0^{2\pi}\int_0^{\pi}\mathbf{M}_{emn}\mathbf{M}_{emn'}\sin\theta d\theta d\phi = \int_0^{2\pi}\int_0^{\pi}\mathbf{M}_{omn}\mathbf{M}_{omn'}\sin\theta d\theta d\phi = 0,\\ \int_0^{2\pi}\int_0^{\pi}\mathbf{N}_{emn}\mathbf{N}_{emn'}\sin\theta d\theta d\phi = \int_0^{2\pi}\int_0^{\pi}\mathbf{N}_{omn}\mathbf{N}_{omn'}\sin\theta d\theta d\phi = 0,\end{aligned} \tag{B.5}$$

when $n \neq n'$ and $m \neq 0$, we need to show that [27]

$$\int_0^{\pi}\left(\frac{dP_n^m}{d\theta}\frac{dP_{n'}^m}{d\theta} + m^2\frac{P_n^m dP_{n'}^m}{\sin^2\theta}\right)\sin\theta d\theta = 0. \tag{B.6}$$

Since the associated Legendre functions satisfy the scalar wave equation

$$\frac{1}{\sin\theta}\frac{d}{d\theta}\left(\sin\theta\frac{d\Theta}{d\theta}\right) + \left[n(n+1) - \frac{m^2}{\sin^2\theta}\right]\Theta = 0, \tag{B.7}$$

we can interpret that

$$\begin{aligned}2\sin\theta\left(\frac{dP_n^m}{d\theta}\frac{dP_{n'}^m}{d\theta} + m^2\frac{P_n^m dP_{n'}^m}{\sin^2\theta}\right) =& 2n(n+1)P_n^m dP_{n'}^m\sin\theta\\ &+ \frac{d}{d\theta}\left(\sin\theta\frac{dP_{n'}^m}{d\theta}P_n^m + \sin\theta\frac{dP_n^m}{d\theta}P_{n'}^m\right).\end{aligned} \tag{B.8}$$

From this and from the orthogonality relations for P_n^m, Eq. B.6 is satisfied. Similarly, when $m = 0$, the orthogonality of M_{emn}, M_{omn}, N_{emn} and N_{omn} can be interpreted using the Eq. B.6 and Eq. B.8.

The property that the vector spherical harmonics form an orthogonal set leads to coefficients of the form [27]:

$$B_{emn} = \frac{\int_0^{2\pi}\int_0^{\pi} \mathbf{E}_i \cdot \mathbf{M}_{emn} \sin\theta \, d\theta \, d\phi}{\int_0^{2\pi}\int_0^{\pi} |\mathbf{M}_{emn}|^2 \sin\theta \, d\theta \, d\phi}. \tag{B.9}$$

Similar expressions can be inferred for B_{omn}, A_{emn}, and A_{omn}. It follows from Eq. 24 that $B_{emn} = A_{omn} = 0$ for all m and n [27]. Furthermore, the other coefficients vanish for $m \neq 1$. Therefore, we obtain

$$\mathbf{E}_i = \sum_{n=1}^{\infty} \left(B_{o1n} \mathbf{M}_{o1n}^{(1)} + A_{e1n} \mathbf{N}_{e1n}^{(1)} \right), \tag{B.10}$$

where the radial dependence of the generating functions is specified as j_n by the superscript (1) on the vector spherical harmonics. This is the only spherical Bessel function that ensures that the incident field is finite at the origin.

The denominator in Eq. B.9 can be evaluated using Eq. B.8. We consider the numerator of the relevant expression which involves the following integral:

$$\int_0^{\pi} \frac{d}{d\theta} \left(\sin\theta P_n^1 \right) e^{ip\cos\theta} \, d\theta. \tag{B.11}$$

From the definition of associated Legendre functions in Eq. B.4, we see that

$$P_n^1 = -\frac{dP_n}{d\theta}. \tag{B.12}$$

Moreover, the Legendre polynomials $P_n(\cos\theta)$ satisfy Eq. B.7

$$\frac{d}{d\theta} \left(\sin\theta \frac{dP_n}{d\theta} \right) = -n(n+1) P_n \sin\theta. \tag{B.13}$$

Using these relations, we find that the integrand in Eq. B.11 is proportional to

$$\int_0^{\pi} e^{ip\cos\theta} P_n \sin\theta \, d\theta. \tag{B.14}$$

This integral is recognized as part of the Gegenbauer generalization of Poisson's integral [27]. The spherical Bessel function $j_n(\rho)$ can be written as

$$j_n(\rho) = \frac{i^{-n}}{2} \int_0^{\pi} e^{i\rho\cos\theta} P_n \sin\theta \, d\theta. \tag{B.15}$$

Combining these results, we directly obtain the expansion coefficient:

$$B_{o1n} = i^n E_0 \frac{2n+1}{n(n+1)}. \tag{B.16}$$

The evaluation of the expansion coefficients A_{e1n} is somewhat more involved than that of B_{01n}. As an example, consider the integral

$$\int_0^\pi P_n^1 \sin\theta \, e^{ip\cos\theta} \sin\theta \, d\theta, \tag{B.17}$$

which can be handled via integration by parts. Using the relations for P_n^1, the Legendre differential identity, and the known integral form of $j_n(\rho)$, we obtain the following:

$$\frac{2n(n+1)}{ip} \, j_n(\rho) \, i^n. \tag{B.18}$$

A more challenging term involves the integral:

$$\int_0^\pi \left(\cos\theta \, \frac{dP_n^1}{d\theta} + \frac{P_n^1}{\sin\theta} \right) e^{ip\cos\theta} \sin\theta \, d\theta, \tag{B.19}$$

which can be simplified by first multiplying the integral form of $j_n(\rho)$ by ρ, and then differentiating with respect to ρ. After some algebraic manipulation, the result becomes

$$\frac{2n(n+1)}{\rho} \, i^n \, \frac{d}{d\rho} \left(\rho j_n \right). \tag{B.20}$$

Using this, the expansion coefficients are readily obtained as

$$A_{e1n} = -iE_0 \, i^n \, \frac{2n+1}{n(n+1)}. \tag{B.21}$$

The plane wave can thus be completely expressed using vector spherical harmonics as

$$\mathbf{E}_i = E_0 \sum_{n=1}^{\infty} i^n \, \frac{2n+1}{n(n+1)} \left(\mathbf{M}_{o1n}^{(1)} - i\mathbf{N}_{e1n}^{(1)} \right). \tag{B.22}$$

References

[1] V. Sasikala and K. Sitra, "All optical switching and associated technologies: a review", Journal of Optics **47**, 307–317 (2018).

[2] B. Real, C. Cantillano, D. López-González, A. Szameit, M. Aono, M. Naruse, S.-J. Kim, K. Wang, and R. A. Vicencio, "Flat-band light dynamics in stub photonic lattices", Scientific Reports **7**, 15085 (2017).

[3] L. Tang, D. Song, S. Xia, S. Xia, J. Ma, W. Yan, Y. Hu, J. Xu, D. Leykam, and Z. Chen, "Photonic flat-band lattices and unconventional light localization", Nanophotonics **9**, doi:10.1515/nanoph-2020-0043 (2020).

[4] V. A. J. Pyykkönen, G. Salerno, J. Kähärä, and P. Törmä, "All-optical switching at the two-photon limit with interference-localized states", Phys. Rev. Res. **5**, 043259 (2023).

[5] Z. Chai, X. Hu, F. Wang, X. Niu, J. Xie, and Q. Gong, "Ultrafast all-optical switching", Advanced Optical Materials **5**, 1600665 (2017).

[6] D. A. B. Miller, "Quantum-well devices for optics in digital systems", in Microelectronic interconnects and packages: optical and electrical technologies, Vol. 1389, edited by G. Arjavalingam and J. Pazaris (International Society for Optics and Photonics, 1991), pp. 496–502.

[7] F. Zhang, L. He, H. Zhang, L.-J. Kong, X. Xu, and X. Zhang, "Experimental realization of topologically-protected all-optical logic gates based on silicon photonic crystal slabs", https://doi.org/10.48550/arXiv.2305.10194 (2023).

[8] J. Clark and G. Lanzani, "Organic photonics for communications", Nature Photonics **4**, https://doi.org/10.1038/nphoton.2010.160 (2010).

[9] N. Wu, Y. Sun, J. Hu, C. Yang, Z. Bai, F. Wang, X. Cui, S. He, Y. Li, C. Zhang, K. Xu, J. Guan, S. Xiao, and Q. Song, "Intelligent nanophotonics: when machine learning sheds light", eLight **5**, https://doi.org/10.1186/s43593-025-00085-x (2025).

[10] Y. Yea, T. Song, Y. Xie, and C. Li, "Design of all-optical subtractors utilized with plasmonic ring resonators for optical computing", Photonics **10**, https://doi.org/10.3390/photonics10070724 (2023).

[11] X. Gai, D.-Y. Choi, S. Madden, and B. Luther-Davies, "Materials and structures for nonlinear photonics", in *All-optical signal processing: data communication and storage applications* (Springer International Publishing, Cham, 2015), pp. 1–33.

[12] W. Yoshiki and T. Tanabe, "All-optical switching using kerr effect in a silica toroid microcavity", Opt. Express **22**, 24332–24341 (2014).

[13] S. Fan, "Sharp asymmetric line shapes in side-coupled waveguide-cavity systems", Applied Physics Letters **80**, 908–910 (2002).

[14] M. F. Yanik, S. Fan, and M. Soljačić, "High-contrast all-optical bistable switching in photonic crystal microcavities", Applied Physics Letters **83**, 2739–2741 (2003).

[15]K. M. Dani, Z. Ku, P. C. Upadhya, R. P. Prasankumar, S. R. J. Brueck, and A. J. Taylor, "Subpicosecond optical switching with a negative index metamaterial", Nano Letters **9**, PMID: 19737005, 3565–3569 (2009).

[16]O. Wada, "Femtosecond all-optical devices for ultrafast communication and signal processing", New Journal of Physics **6**, 183 (2004).

[17]A. Pasquazi, S. Stivala, G. Assanto, V. Amendola, M. Meneghetti, M. Cucini, and D. Comoretto, "In situ tuning of a photonic band gap with laser pulses", Applied Physics Letters **93**, 091111 (2008).

[18]P. Tran, "Optical limiting and switching of short pulses by use of a nonlinear photonic bandgap structure with a defect", J. Opt. Soc. Am. B **14**, 2589–2595 (1997).

[19]D. Leykam, A. Andreanov, and S. Flach, "Artificial flat band systems: from lattice models to experiments", Advances in Physics: X **3**, 1473052 (2018).

[20]B. Sutherland, "Localization of electronic wave functions due to local topology", Phys. Rev. B **34**, 5208–5211 (1986).

[21]A. Mielke, "Ferromagnetic ground states for the hubbard model on line graphs", Journal of Physics A: Mathematical and General **24**, L73 (1991).

[22]H. Tasaki, "Ferromagnetism in the hubbard models with degenerate single-electron ground states", Phys. Rev. Lett. **69**, 1608–1611 (1992).

[23]G. Centała and J. W. Kłos, "Compact localized states in magnonic lieb lattices", Scientific Reports **13**, 10.1038/s41598-023-39816-w (2023).

[24]R. A. Vicencio, C. Cantillano, L. Morales-Inostroza, B. Real, C. Mejıa-Cortés, S. Weimann, A. Szameit, and M. I. Molina, "Observation of localized states in lieb photonic lattices", Phys. Rev. Lett. **114**, 10.1103/PhysRevLett.114.245503 (2015).

[25]P. Törmä, S. Peotta, and B. A. Bernevig, "Superconductivity, superfluidity and quantum geometry in twisted multilayer systems", Nature Reviews Physics **4**, 528–542 (2022).

[26]M. Mazilu, "Mie scattering eigenmodes for optical trapping", https://doi.org/10.48550/arXiv.1704.08779 (2017).

[27]C. Bohren and D. Huffman, "Absorption and scattering of light by small particles", John Wiley Sons, Ltd, https://doi.org/10.1002/9783527618156.fmatter (1998).

[28]U. Dixit, "Finite element methods in engineering", (2007).

[29]*COMSOL multiphysics: wave optics module user's guide, version 6.0*, COMSOL AB (Stockholm, Sweden, 2021).

[30]A. Zalogina, L. Carletti, and A. Rudenko, "High-harmonic generation from a subwavelength dielectric resonator", Science Advances **9**, 10.1126/sciadv.adg2655 (2023).

[31] A. C. Tasolamprou, O. Tsilipakos, M. Kafesaki, C. M. Soukoulis, and E. N. Economou, "Toroidal eigenmodes in all-dielectric metamolecules", Phys. Rev. B **94**, 205433 (2016).

[32] D. Raventós, T. Graß, M. Lewenstein, and B. Juliá-Díaz, "Cold bosons in optical lattices: a tutorial for exact diagonalization", Journal of Physics B: Atomic, Molecular and Optical Physics **50**, 113001 (2017).

[33] Jaakko Kähärä, *Bosonic switching in flat bands* (Master thesis, University of Helsinki, 2022).

[34] D. A. B. Miller, D. S. Chemla, D. J. Eilenberger, P. W. Smith, A. C. Gossard, and W. Wiegmann, "Degenerate four-wave mixing in room-temperature gaas/gaalas multiple quantum well structures", Applied Physics Letters **42**, 10.1063/1.93802 (1983).